Simultaneous System Calibration of a Multi-LiDAR Multicamera Mobile Mapping Platform

Radhika Ravi ⓘ, Yun-Jou Lin, Magdy Elbahnasawy ⓘ, Tamer Shamseldin ⓘ, and Ayman Habib

Abstract—Mobile light detection and ranging (LiDAR) systems are widely used to generate precise 3-D spatial information, which in turn aids a variety of applications such as digital building model generation, transportation corridor asset management, telecommunications, precision agriculture, and infrastructure monitoring. Integrating such systems with one or more cameras would allow forward and backward projection between imagery and LiDAR data, thus facilitating several other high-level data processing activities, such as reliable feature extraction and colorization of point cloudsv. To increase the registration accuracy of point clouds derived from LiDAR data and imagery, along with their accuracy with respect to the ground truth, a simultaneous estimation of the mounting parameters relating the different laser scanners and cameras to the onboard global navigation satellite system (GNSS)/inertial navigation system (INS) unit is vital. This paper proposes a calibration procedure that directly estimates the mounting parameters for several spinning multibeam laser scanners and cameras onboard an airborne or terrestrial mobile platform. This procedure is based on the use of conjugate points and linear/planar features in overlapping images and point clouds derived from different drive-runs/flight lines. In order to increase the efficiency of semi-automatic conjugate feature extraction from the LiDAR data, specifically designed calibration boards covered by highly reflective surfaces that could be easily deployed and set up within an outdoor environment are used in this study. An experimental setup is used to evaluate the performance of the proposed calibration procedure for both airborne and terrestrial mobile mapping systems through the *a posteriori* variance factor of the least squares adjustment procedure and the quality of fit of the adjusted LiDAR point cloud and image points to linear/planar surfaces before and after the calibration process.

Index Terms—Calibration, cameras, least squares adjustment (LSA), mobile light detection and ranging (LiDAR) systems.

I. INTRODUCTION

LIGHT detection and ranging (LiDAR) units use laser beams to measure ranges and generate precise 3-D information about the scanned area. Such units can be placed on airborne platforms (such as UAVs) or terrestrial platforms (such

as cars or trucks). The ideal platform for conducting a survey is dependent on the desired application. For instance, an airborne LiDAR system is more suitable for precision agriculture, digital building model generation, or accident-scene reconstruction. However, a mobile terrestrial LiDAR system would be preferred for infrastructure monitoring and transportation corridor asset management. Currently, there are commercially available LiDAR units that are capable of emitting more than a quarter million pulses per second at a cost of less than $10k. Such availability, together with the ever-increasing range of applications, has led to the widespread use of mobile LiDAR systems [1]–[4]. Furthermore, such systems could be integrated with several cameras in order to obtain additional information. However, the attainment of the full 3-D point positioning potential of such systems is contingent on an accurate calibration of the mobile mapping unit as a whole. Over the past few years, extensive research has been conducted for the calibration of airborne and terrestrial mobile mapping systems consisting of laser scanners [5]–[7]. Muhammad and Lacroix [8] performed calibration of a rotating multibeam LiDAR with the objective to align the scan data as close as possible to a ground truth environment. He *et al*. [9] used pairwise multitype 3-D geometric features (i.e., points, lines, and planes) to derive the extrinsic calibration parameters between a 2-D LiDAR and GPS/IMU. First, the points were segmented into different features and their quality was evaluated to compute weights to be used in the minimization of the normal distance between conjugate features. Similarly, several techniques have been developed to accurately calibrate different types of cameras in order to obtain accurate estimates of their intrinsic and extrinsic parameters. Weng *et al.* [10] proposed a two-step stereo camera calibration procedure to obtain the intrinsic parameters and the exterior orientation parameters of the involved cameras. The first step aimed to obtain the calibration parameters using a closed-form solution by assuming a distortion-free camera model. Then, the parameters obtained in the first step were improved iteratively through a nonlinear optimization, taking into account camera distortions. Zhang [11] proposed a technique for camera calibration using a planar pattern captured by a camera from different orientations. This approach used a closed-form solution, followed by a nonlinear refinement based on the maximum likelihood criterion. Habib *et al.* [12] and Furukawa and Ponce [13] devised a bundle adjustment of images for an accurate camera calibration to obtain its intrinsic and extrinsic parameters with the help of tie points and linear features. Delara *et al.* [14] further suggested the incorporation of LiDAR data as control points within the bundle

adjustment. Habib *et al.* [15] suggested alternative approaches for the registration of data captured by LiDAR and photogrammetric systems using a set of linear features by applying a bundle adjustment followed by a similarity transformation.

Although many procedures have been developed for LiDAR system calibration and camera calibration separately, the simultaneous calibration of a mapping system consisting of both LiDAR units and cameras is an area of research that is still under exploration. Zhang and Pless [16] performed an extrinsic calibration of a camera and a 2-D laser range finder by observing a planar checkerboard pattern and solving for constraints between the views from both of these devices. This was done by first determining the pose of the camera with respect to the calibration plane, which was further used to estimate the normal direction for the planar pattern in the camera coordinate system. Then, the extrinsic parameters, i.e., the rigid transformation from the camera coordinate system to the laser coordinate system, were obtained by constraining the points (belonging to the planar pattern) captured by the laser scanner to lie on the planar pattern estimated from the camera image. Fremont and Bonnifait [17] proposed an approach for extrinsic calibration of a camera and a 3-D laser range finder using a circle-based calibration object. First, an initial estimate of the rigid transformation between the camera and laser unit coordinate systems was obtained through parametrizing the calibration target by the 3-D coordinates of the circle center and the normal vector of its plane. Then, a nonlinear 3-D minimization was carried out in order to refine the estimated extrinsic parameters. Castorena *et al.* [18] devised a method for automatic extrinsic calibration and sensor fusion for a system comprised of a LiDAR and an optical camera by exploiting the natural alignment of depth and intensity edges. However, this approach demands the availability of depth maps and intensity images for accurate calibration and cannot be applied in case of an unavailability of either of the information. Le and Ng [19] proposed an approach for calibrating multiple sensors (cameras, laser unit, and robot arm) by grouping them such that each group outputs 3-D data. Their approach uses geometric constraints (distance preservation, collinearity, and coplanarity constraints) applied to 3-D data in order to estimate the extrinsic parameters relating the different sensors of a robotic system. However, their calibration approach was designed for stationary systems, and moreover, their framework was built upon 3-D systems. For instance, two cameras onboard a system were grouped to form a stereo vision system that outputs 3-D data. On the other hand, the calibration approach proposed in the current paper deals with directly georeferenced mobile systems and it can estimate the extrinsic parameters for single or multiple cameras without having a need to group them to create 3-D systems. Levinson and Thrun [20] devised an approach for real-time miscalibration detection and correction. Any sudden miscalibration was detected using a probabilistic background monitoring algorithm and any gradual drift in sensor parameters was tracked and adjusted by observing the change in the objective function over past few frames of data capture. Although their approach can accurately detect small incremental values to attain accurate calibration, they have not addressed the issue of accurate calibration starting with significantly inaccurate initial estimates for the parameters. However, this problem is mitigated by the

proposed calibration approach where we demonstrate that it can attain accurate calibration results even on starting with inaccurate estimates. A detailed literature review has been conducted in the field of LiDAR–camera calibration and the characteristics and limitations of these papers are summarized as follows.

1) The calibration approaches suggested in [16], [17], and [21]–[30] rely on the usage of specifically designed targets of known dimensions in order to attain accurate results. On the other hand, Pandey *et al.* [31]–[33] propose a targetless calibration strategy exploiting the features available in surrounding environment.

2) Most of the proposed calibration techniques use exact point-to-point correspondences. For instance, in [17] and [21], 3-D–3-D point correspondences are used; in [22], [23], [26]–[28], and [30]–[32], 2-D–3-D point correspondences are used, and in [16], [24], and [29], 2-D–2-D point correspondences are used. However, Gong *et al.* [33] do not rely on exact point-to-point correspondences for calibration.

3) The LiDAR–camera calibration techniques in [16], [17], [22]–[25], [28], [29], and [31] are developed only for systems consisting of a single LiDAR and a single camera. But, the techniques of [21], [27], [30], and [32] are applicable for systems with a single LiDAR and multiple cameras. The approaches proposed in [26] and [33] are capable of calibrating systems with multiple LiDAR units and multiple cameras.

4) Several calibration approaches, such as the ones proposed in [16], [24], and [29] only target the calibration of systems with 2-D LiDAR units, whereas other approaches [17], [21]–[23], [25], [26]–[28], [30]–[33] are developed for 3-D LiDAR units.

5) The approaches in [16], [17], [21], [22], and [24]–[30] are indoor calibration approaches, whereas in [23], [31], and [32] are outdoor calibration approaches. However, Gong *et al.* [33] present an approach that can be used for indoor as well as outdoor calibration.

6) Most of the papers [16], [17], [21], [22], [24]–[30], [33] propose calibration techniques for stationary systems, which do not have a global navigation satellite system (GNSS)/inertial navigation system (INS) unit onboard. On the other hand, García-Moreno *et al.* [23], Pandey *et al.* [31], and Bileschi [32] use mobile mapping systems with an onboard GNSS/INS unit but they do not address the extrinsic calibration of the sensors with respect to the GNSS/INS unit, thus resulting in a partial calibration of the system.

7) In [16], [21], [23], [24], [27]–[29], and [31], single-step calibration techniques are proposed, whereas in [17], [22], [25], [26], [30], [32], and [33], multistep calibration approaches are proposed.

8) The papers [16], [17], [21], [23]–[27], [31], [33] only deal with the calibration of extrinsic parameters relating the LiDAR units and cameras. Only [22] accounts for intrinsic LiDAR parameters along with the extrinsic calibration parameters relating LiDAR and camera. In [28]–[30] and [32], the intrinsic camera parameters as well as the extrinsic LiDAR–camera parameters are estimated.

9) The papers [16], [17], [21], [22], [24]–[33] include a built-in quality control strategy to estimate the accuracy of the proposed calibration approaches, whereas [23] lacks any information about the quality of the obtained calibration results.

The current research focuses on a potential generic calibration technique for a mobile mapping system with several spinning multibeam laser scanners and cameras onboard an airborne or terrestrial platform. The focus of the system calibration is to simultaneously estimate the mounting parameters relating the individual laser scanners, cameras, and the onboard GNSS/INS unit using an iterative calibration procedure that minimizes the discrepancy between conjugate points and linear/planar features in overlapping point clouds and images derived from different drive-runs/flight lines. The simultaneous estimation of all the mounting parameters would increase the registration accuracy of the point clouds derived from LiDAR and photogrammetric data. This would also allow for forward and backward projection between image and LiDAR data, which in turn is useful for high-level data processing activities, such as object or feature extraction.

The major contributions of our paper that significantly overcome the limitations of the state-of-the-art techniques are as follows.

1) In our approach, there is no requirement of any specially designed calibration targets with known properties in order to conduct an accurate calibration. Instead, the calibration can be done using any planar/linear features and distinctly identifiable points available in the surrounding environment, such as building facades, rooftops, traffic sign boards, light poles, and so on.

2) Since we propose a feature-based calibration technique, our approach does not necessarily require exact point-to-point correspondences of any type (2D–2D, 2D–3D, or 3D–3D). Instead, our approach uses pseudo-conjugate points belonging to conjugate features that can be easily extracted from LiDAR and camera.

3) Our proposed calibration approach is capable of simultaneously estimating the extrinsic parameters relating an arbitrary number of sensors (LiDAR units and cameras), i.e., it has no such restriction that it would work only for single LiDAR-single camera systems. Moreover, this approach is generic to be applied to terrestrial and airborne mapping systems alike—an aspect that has not been addressed in any of the previous works.

4) We propose a sensor-independent calibration model, i.e., it is independent of whether the mapping system consists of a single-beam or a multibeam LiDAR, 2-D or 3-D laser scanner, and whether a camera is a frame or a line camera. The calibration for any combination of any type of these sensors can be achieved using the proposed calibration technique without making any modification to the model.

5) Our approach is flexible to the type of the mapping system being used, i.e., the calibration approach can be applied to stationary as well as mobile mapping systems alike. In case of mobile mapping systems, our approach relies on the availability of a GNSS/INS

unit and we propose a single-step complete calibration technique that can estimate the extrinsic calibration relating any combination of the mentioned sensors, i.e., LiDAR–LiDAR, LiDAR–camera, camera–camera, LiDAR–GNSS/INS, and/or camera–GNSS/INS, simultaneously. Similarly, it is also applicable to indoor as well as outdoor mapping systems.

6) Although our paper only addresses the estimation of extrinsic parameters relating the various onboard sensors, it is worth mentioning that our model is also capable of simultaneously estimating the intrinsic parameters of the different sensors since the model deals directly with raw measurements obtained from different modalities.

7) Our paper also validates the accuracy of the proposed strategy by conducting an extensive qualitative evaluation by studying the registration of the data obtained from different modalities in the 3-D object space as well as 2-D image space. Moreover, a thorough quantitative evaluation is also reported by listing the confidence interval of the estimated parameters, the quality of fit for different calibration features, and the comparison of results to the expected error derived using error propagation calculation.

Apart from the above-mentioned characteristics, the assumptions and limitations of our proposed calibration approach, which serve as the basis for our future work, are summarized as follows.

1) Although the calibration approach is capable of dealing with stationary as well as mobile systems, in case of mobile mapping systems, our approach relies on the availability of sufficiently accurate GNSS/INS position and orientation information. However, if such information is not available at an acceptable accuracy, our approach has the ability to detect this issue by analyzing the fitting residuals for different features.

2) Since the previously developed calibration techniques mostly rely on specifically designed calibration targets, these approaches facilitate the automatic extraction of such features. However, the limitation of this paper is the manual efforts involved in certain steps, such as selection of seed points and bounding points for various features during feature extraction from LiDAR data and the manual image coordinate measurement for the various calibration features captured by the cameras. This can be attributed to the flexibility provided in the choice of features being used for calibration.

3) Although the proposed calibration model can be used to simultaneously estimate the intrinsic parameters of the different sensors (LiDAR and camera) along with the extrinsic parameters, this work still does not address the development of an optimal/minimal track and target configuration in order to derive accurate estimates of all these parameters. Hence, the experimental results included in this paper only focus on the estimation of extrinsic parameters.

In this paper, we first discuss the 3-D point positioning equations used for multiunit LiDAR system and GNSS/INS-assisted
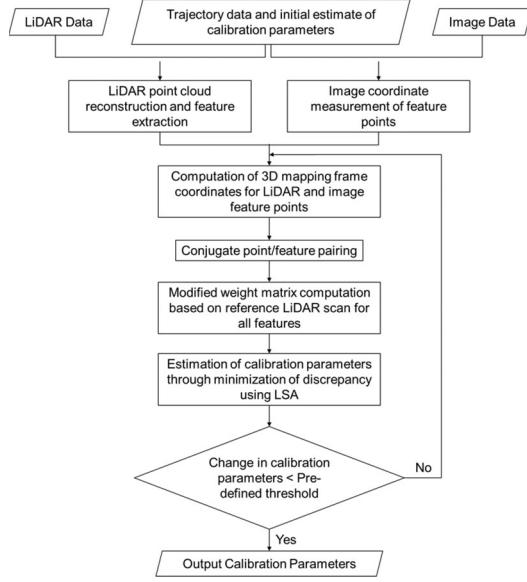
Fig. 1.   Flowchart of the steps involved in the proposed calibration strategy.

multicamera system. Next, we compare the proposed point-pairing-based triangulation approach with the conventional bundle adjustment based model. Then, the representation scheme and extraction of linear and planar features in LiDAR scans and images are discussed. An optimal pairing scheme is developed based on an analysis of the contribution of incorporating both LiDAR and image points belonging to these features toward the estimation of calibration parameters. Finally, an iterative calibration procedure is proposed and its performance is evaluated using experimental datasets collected using an airborne and two different terrestrial mobile mapping platforms. The results are qualitatively evaluated in the mapping frame (3-D alignment) as well as the image space (2-D alignment). The accuracy of the calibration procedure is quantified by the *a posteriori* variance factor of the least squares adjustment (LSA) procedure and the quality of fit of the adjusted point clouds to planar surfaces and linear features before and after the calibration process. The accuracy obtained after calibration is also compared to the expected accuracy from error propagation according to the specifications of the system components (laser scanners, cameras, and geo-referencing units).

II. METHODOLOGY FOR MULTI-LIDAR MULTICAMERA SYSTEM CALIBRATION

The conceptual basis for multi-LiDAR multicamera system calibration is to minimize the discrepancies among conjugate points, linear features, and/or planar features obtained from different laser scanners, cameras, and/or drive-runs/flight lines. Fig. 1 shows a flowchart listing the steps involved in calibration. Each of these steps is discussed in more detail in the forthcoming sections.

A. Conceptual Basis of a Multiunit LiDAR Point Positioning

A typical LiDAR system consisting of spinning multibeam laser scanners could involve three coordinate systems (i.e.,
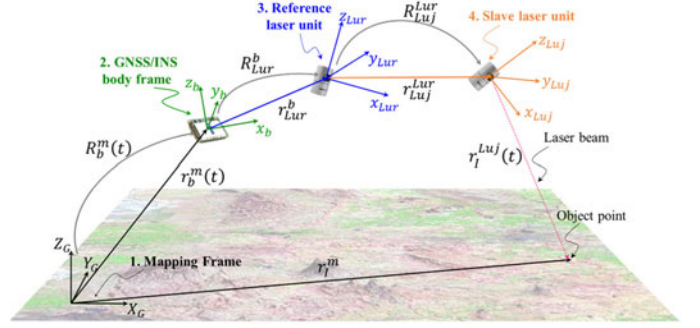

Fig. 2.   Illustration of point positioning of a multiunit LiDAR system.

mapping frame, IMU body frame, and laser unit frame). A given point I acquired from a mobile mapping system equipped with multiple laser scanners can be reconstructed in the mapping coordinate system using (1), which is graphically illustrated in Fig. 2. The vector and matrix notations used in this paper are as follows.

1) r_a^b denotes the coordinates of point "a" relative to point "b" in the coordinate system associated with point "b."
2) R_a^b denotes the rotation matrix that transforms a vector-defined relative to the coordinate system "a" into a vector-defined relative to the coordinate system "b."

For the laser unit frame, the origin is defined at the laser beams firing point and the z-axis is along the axis of rotation of the laser unit. For a spinning multibeam laser scanner, each laser beam is fired at a fixed vertical angle β; the horizontal angle α is determined based on the rotation of the unit; and the range ρ is derived from the time of flight between the firing point and the laser beam footprint. So, the coordinates of a 3-D point relative to the laser unit coordinate system $r_I^{luj}(t)$ are defined by (2). For a multiunit LiDAR system, one of the laser scanners is set as reference and the rest are considered to be slave sensors. The reference sensor (lur) is related to the IMU body frame by a rigidly defined lever arm r_{lur}^b and boresight matrix R_{lur}^b. Similarly, each slave sensor (luj) is related to the reference one (lur) by a rigidly defined lever arm r_{luj}^{lur} and boresight matrix R_{luj}^{lur}. The GNSS/INS integration provides the time-dependent position $r_b^m(t)$ and rotation $R_b^m(t)$ relating the mapping frame and IMU body frame coordinate systems. One should note that such a LiDAR system can also be modeled by directly relating each of the laser scanners to the IMU body frame but the current model is preferred due to the fact that it allows for the derivation of the mounting parameters relating the slave sensors to the reference one without the need for GNSS/INS position and orientation information:

$$r_I^m = r_b^m(t) + R_b^m(t)\, r_{lur}^b + R_b^m(t)\, R_{lur}^b\, r_{luj}^{lur}$$
$$+ R_b^m(t)\, R_{lur}^b\, R_{luj}^{lur}\, r_I^{luj}(t) \tag{1}$$

$$r_I^{luj}(t) = \begin{pmatrix} x \\ y \\ z \end{pmatrix} = \begin{pmatrix} \rho(t)\cos\beta(t)\cos\alpha(t) \\ \rho(t)\cos\beta(t)\sin\alpha(t) \\ \rho(t)\sin\beta(t) \end{pmatrix}. \tag{2}$$
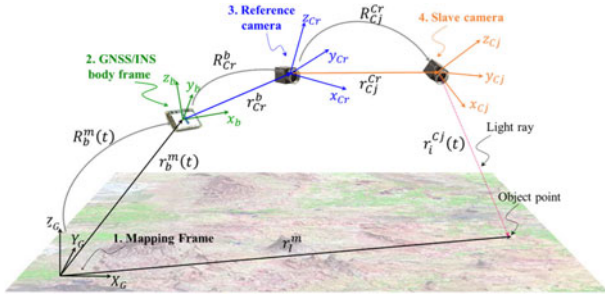
Fig. 3. Illustration of point positioning of a GNSS/INS-assisted multicamera system.

B. Point Positioning for a GNSS/INS-Assisted Multicamera System

A typical GNSS/INS-assisted multicamera system involves three coordinate systems (i.e., mapping frame, IMU body frame, and camera coordinate frame). A given point $\boldsymbol{I}$ captured in an image as point $\boldsymbol{i}$ from a mobile mapping system comprising multiple cameras can be reconstructed in the mapping coordinate system using (3), which is graphically illustrated in Fig. 3.

For the camera coordinate frame, the origin is defined at the perspective center and the x, y-axes are defined along the direction of the rows and columns of the image, respectively. So, the coordinates of a point $\boldsymbol{i}$ in an image captured by camera Cj relative to the camera coordinate system $r_i^{Cj}(t)$ are defined by (4). Here, x_{pj} and y_{pj} denote the location of the principal point, f_j denotes the principal distance, and $\text{dist}_{x_{ij}}$ and $\text{dist}_{y_{ij}}$ denote the distortion in image coordinate measurements for point $\boldsymbol{i}$ in the jth camera. These intrinsic parameters $(x_{pj}, y_{pj}, f_j, \text{dist}_{x_{ij}}, \text{dist}_{y_{ij}})$ are known *a priori* for a calibrated camera. For a multicamera system, one of the cameras is set as reference and the rest are considered to be slave cameras. The reference camera (Cr) is related to the IMU body frame by a rigidly defined lever arm r_{Cr}^b and boresight matrix R_{Cr}^b. Similarly, each slave camera (Cj) is related to the reference one (Cr) by a rigidly defined lever arm r_{Cj}^{Cr} and boresight matrix R_{Cj}^{Cr}. Finally, each point $\boldsymbol{i}$ in an image captured by camera C_j at time t has a scaling factor associated with it, which is denoted by $\lambda(i, Cj, t)$:

$$r_I^m = r_b^m(t) + R_b^m(t) r_{Cr}^b + R_b^m(t) R_{Cr}^b r_{Cj}^{Cr}$$
$$+ \lambda(i, Cj, t) R_b^m(t) R_{Cr}^b R_{Cj}^{Cr} r_i^{Cj}(t) \quad (3)$$

$$r_i^{Cj}(t) = \begin{pmatrix} x_{ij} - x_{pj} - \text{dist}_{x_{ij}} \\ y_{ij} - y_{pj} - \text{dist}_{y_{ij}} \\ -f_j \end{pmatrix}. \quad (4)$$

In case of a conventional photogrammetric bundle adjustment for single/multicamera systems, (3) is modified in order to eliminate the scaling factor. The terms in the equation are first rearranged to produce (5), which is further simplified to result in (6a) and (6b), where the scaling factor has been eliminated by reducing three equations to two. In this model, the unknowns involved for an image point are its 3-D mapping frame coordinates r_I^m (assuming that the intrinsic camera parameters, GNSS/INS position and orientation, and intersensor mounting parameters

are available). So, if a point $\boldsymbol{I}$ is observed in m different images, then based on this model, there will be a total of $2m$ equations in three unknowns (r_I^m), thus resulting in a point definition redundancy of $(2m - 3)$:

$$r_i^{Cj}(t) = \frac{1}{\lambda(i, Cj, t)} \left[R_{Cr}^{Cj} R_b^{Cr} R_m^b(t) \left[r_I^m - r_b^m(t) \right] \right.$$
$$\left. - R_{Cr}^{Cj} R_b^{Cr} r_{Cr}^b - R_{Cr}^{Cj} r_{Cj}^{Cr} \right] = \frac{1}{\lambda(i, Cj, t)} \begin{bmatrix} N_x \\ N_y \\ D \end{bmatrix}$$
$$(5)$$

$$x_{ij} = x_{pj} - f_j \frac{N_x}{D} + \text{dist}_{x_{ij}} \quad (6a)$$

$$y_{ij} = y_{pj} - f_j \frac{N_y}{D} + \text{dist}_{y_{ij}}. \quad (6b)$$

In this research, we propose a new approach for bundle adjustment that uses point pairings between various image points. This model is introduced in the forthcoming section and also compared to the conventional bundle adjustment to examine the equivalency of the two models in terms of their parameter estimation ability.

C. New Point-Pairing-Based Bundle Adjustment and Its Comparison to the Conventional Model

We propose a point-pairing-based bundle adjustment where (3) is retained in its original form, i.e., the scaling factors are not eliminated by reducing the three equations to two. Rather, the scaling factors are treated as unknowns to be estimated. This model aims to eliminate the 3-D mapping frame coordinates of a point in order to allow for the estimation of scaling factors for the corresponding image points along with the calibration parameters. This is achieved by imposing an equality constraint on the 3-D mapping frame coordinates computed for different image points representing the same object point by pairing them together. For instance, for a point $\boldsymbol{I}$ captured in two different images—one by camera Cj at time t_1 and another by camera C_k at time t_2—the difference between the mapping coordinates computed from both images should be zero, (7). Here, the unknowns include the scaling factors for the two image points $\lambda(i, Cj, t_1)$ and $\lambda(i', Ck, t_2)$. So, if a point $\boldsymbol{I}$ is observed in m different images, then based on this model, there will be a total of $(m - 1)$ independent pairings between the images, where each pairing would result in three equations and each image point will have an associated scaling factor. Hence, there will be a total of $3(m - 1)$ equations in m unknowns (scaling factors), thus resulting in a point definition redundancy of $(2m - 3)$. This is the same as that obtained for the conventional model for bundle adjustment. The identical point definition redundancy, in turn, proves the equivalency of the traditional model and the proposed point-pairing-based bundle adjustment. In this research, we use the latter model as it facilitates having a direct expression of the 3-D mapping frame coordinates for the image points so that they can also be paired with the corresponding LiDAR points; as will be discussed in the forthcoming sections

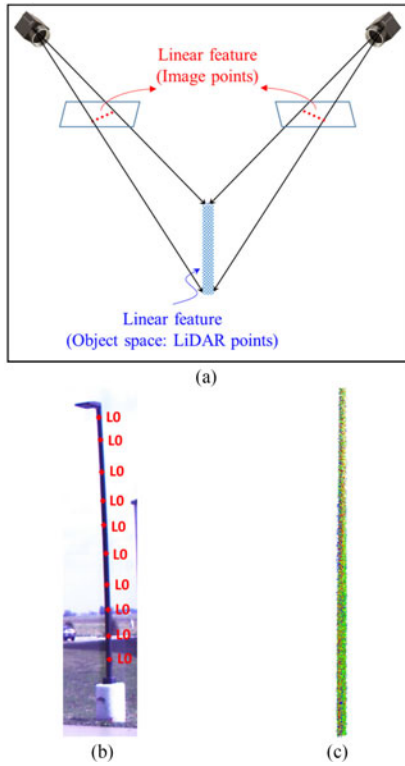$$r_I^m(i, Cj, t_1) - r_I^m(i', Ck, t_2) = 0. \quad (7)$$

Fig. 4. Representation of linear features in imagery and LiDAR data. (a) Schematic illustration. (b) Image points along a light pole. (c) LiDAR points along the same light pole.

D. Calibration Strategy for a Multi-LiDAR Multicamera System

A multi-LiDAR multicamera system calibration aims to simultaneously estimate all the system parameters so as to minimize the discrepancies among conjugate points, linear features, and/or planar features obtained from different laser scanners, cameras, and/or drive-runs/flight lines. In order to achieve this, first, we have to devise a feature representation scheme, a feature extraction technique, and an optimal pairing strategy for the different types of features based on their representation in imagery and LiDAR data.

1) Representation Scheme and Feature Extraction: In this section, we discuss the representation scheme used in this study for linear and planar features in imagery and LiDAR data. Furthermore, we describe the semi-automatic feature extraction procedure used to derive various features from LiDAR data.

Linear features: A linear feature appearing in an image or a LiDAR scan is represented by a sequence of pseudo-conjugate points lying along the feature. Here, the term "pseudo-conjugate points" refers to points that are not distinctly identifiable in different images or LiDAR scans but are known to belong to the same feature. The representation of linear features in images and LiDAR data is schematically illustrated in Fig. 4(a) and depicted for a light pole in Fig. 4(b) and (c). Note that points along a linear feature are labeled the same, thus denoting that the points are indistinct in nature, i.e., the only identification of a point is by the feature that it belongs to and there is no assumption about having conjugate points among different images and LiDAR scans.
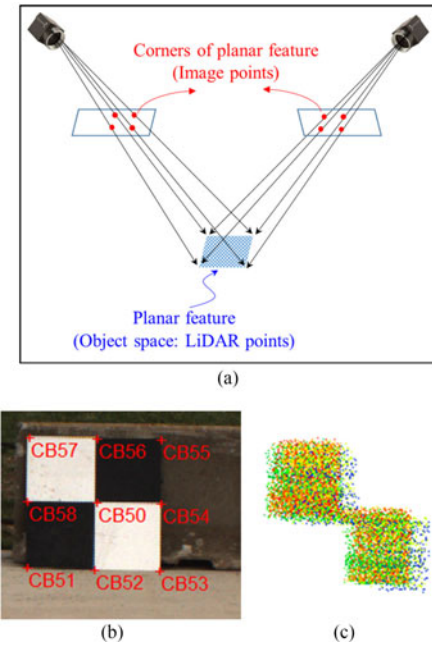

Fig. 5. Representation of planar features in imagery and LiDAR data. (a) Schematic illustration. (b) Image points along a checkerboard target. (c) LiDAR points along the same checkerboard target.

In outdoor calibration, various linear features can be extracted and used, such as flag poles, light poles, physical intersections of neighboring planar features, and so on. Features like flag poles or light poles are extracted from LiDAR data by specifying the two end points. A buffer radius is set to define a cylinder around the linear feature of interest. Then, a line-fitting is done for the points lying within this cylindrical buffer, and finally, the points that lie within a normal distance threshold from the best-fitting line are extracted. On the other hand, points belonging to intersections of neighboring planar features are extracted by first, determining the best-fitting planes for each of the two planar surfaces. Then, their intersection line is determined and all the points lying within a normal distance threshold from this line are extracted. In the case of imagery data, linear features are extracted by manually measuring image coordinates for pseudo-conjugate points along corresponding features.

Planar features: A planar feature appearing in a LiDAR scan is represented by a sequence of pseudo-conjugate points lying along the feature. However, in the case of an image, a planar feature is represented by distinct points, such as the corners, along the feature, as shown schematically in Fig. 5(a). For instance, the representation for a checkerboard target (used in this study) is depicted in Fig. 5(b). Note that LiDAR points belonging to each planar feature will have the same labels (which are specific to the feature) but the corresponding image points (here, corners of a board) will have distinct labels (specific to the corresponding object point). The justification for this deviation in the representation scheme followed for planar features from the one established for linear features is discussed in detail in Section II-D2.

In this study, we use highly reflective boards, ground patches, wall patches, and other surfaces as planar features for

Fig. 6. Intensity data from a point cloud that includes highly reflective boards.

calibration. The highly reflective sign boards can be identified from intensity data, as shown in Fig. 6, where the points belonging to these boards exhibit higher intensity values than other LiDAR points. First, a predefined threshold is set to extract high-intensity points. To avoid the extraction of high-intensity points belonging to objects other than these boards, an approximate preset region is set as seed points for each board. Then, a distance-based region growing technique is adopted to group the high-intensity board returns. Finally, a plane-fitting is done for these points, and the points lying within a normal distance threshold from the best-fitting plane are extracted. Other planar features, such as ground patches, wall patches, and other planar surfaces, are extracted by defining two diagonally opposite corners. A bounding box is constructed around the planar feature of interest by adding a buffer value (in *X*-, *Y*-, and *Z*-directions) to the coordinates of diagonally opposite corners. Again, a plane-fitting is done for the points contained inside the box, and the ones lying within a normal distance threshold from the best-fitting plane are extracted. In the case of imagery data, the image coordinates of distinctly identifiable points along a planar feature (corners or center) are manually measured.

2) Development of an Optimal Pairing Scheme for Calibration: Now that the representation scheme has been established for the different types of features used for calibration, we proceed to analyze their contributions toward calibration. The mapping frame coordinates of a point *I* captured in a LiDAR scan and an image can be derived using (1) and (3), respectively. Consequently, the calibration objective function is to find the system parameters that minimize the discrepancies between the 3-D coordinates of a point derived from different drive-runs/flight lines. In case of a multi-LiDAR multicamera system, these discrepancies can arise from three types of pairings—LiDAR-to-LiDAR pairing [see (8)], image-to-image pairing [see (9)], and LiDAR-to-image pairing [see (10)], where the term pairing refers to a point (say, *I*) observed in two LiDAR scans, two images, or one LiDAR scan and one image:

$$\text{LiDAR - to - LiDAR pairing}: r_I^m(Lu_j, t_1) - r_I^m(Lu_k, t_2) = 0 \tag{8}$$

$$\text{Image - to - image pairing}: r_I^m(C_j, t_1) - r_I^m(C_k, t_2) = 0 \tag{9}$$

$$\text{LiDAR - to - image pairing}: r_I^m(Lu_j, t_1) - r_I^m(C_k, t_2) = 0. \tag{10}$$

Now, the contribution of each of the above-mentioned pairings toward calibration is analyzed for points, linear features, and planar features. One should note that each point pair serves two purposes—first is the derivation of 3-D mapping frame

coordinates of the involved points and second is the estimation of system calibration parameters. So, in order to determine the contribution from a pairing toward system calibration, we compute the point definition redundancy, i.e., the redundancy for the derivation of the 3-D mapping frame coordinates of LiDAR/image points, as a result of LiDAR-to-LiDAR, image-to-image, and LiDAR-to-image pairings.

One should note that in case of a LiDAR point, there are no additional unknowns involved in computing its 3-D mapping frame coordinates apart from the system parameters. However, in case of an image point, there is a unique scaling factor associated with it, which is an additional unknown for computing its 3-D mapping frame coordinates.

Point-based pairings: Let us consider a point *I* captured in *n* different LiDAR scans and *m* different images. Then, there can be a total of $(n-1)$ independent LiDAR-to-LiDAR pairings, $(m-1)$ independent image-to-image pairings, and one additional pairing between a LiDAR scan and an image for this point. Each point pairing will result in a random misclosure vector ($\vec{e}$), as follows:

$$r_I^m \text{ (LiDAR scan/image 1)}$$
$$- r_I^m \text{ (LiDAR scan/image 2)} = \vec{e}. \tag{11}$$

For a conjugate point pairing, the discrepancy ($\vec{e}$) is minimized along the *X*-, *Y*-, and *Z*-directions of the mapping frame, thus resulting in three equations for each point pair. So, a LiDAR-to-LiDAR point pairing will result in three equations with no additional unknowns, and hence, the point definition redundancy is 3. Now, an image-to-image point pairing would introduce a scaling factor corresponding to each image. As a result, there will be three equations and two unknowns, i.e., the point definition redundancy is 1. Similarly, a LiDAR-to-image point pairing will give rise to three equations and one unknown (scaling factor corresponding to the image point), and thus, the point definition redundancy is 2. However, owing to the irregular distribution of LiDAR points, there is no accurate point-to-point correspondence between the LiDAR point clouds and images obtained from different drive-runs/flight lines, thus ruling out the possibility of LiDAR-to-LiDAR and LiDAR-to-image conjugate point pairing.

Linear-feature-based pairings: As discussed before, a linear feature is represented by a sequence of pseudo-conjugate points along the feature. Each pseudo-conjugate point pairing will result in a random misclosure vector ($\vec{e}$) along with a nonrandom misclosure vector ($\vec{D}$), as shown in Fig. 7(a) and expressed mathematically as follows:

$$r_I^m \text{ (LiDAR scan/image 1)}$$
$$- r_J^m \text{ (LiDAR scan/image 2)} = \vec{D} + \vec{e}. \tag{12}$$

In this case, the discrepancy of the resultant point pair should be minimized only along the two directions that are normal to the axial direction of the linear feature, thus resulting in two equations from each pseudo-conjugate point pair. This is achieved by applying a modified weight matrix to the point
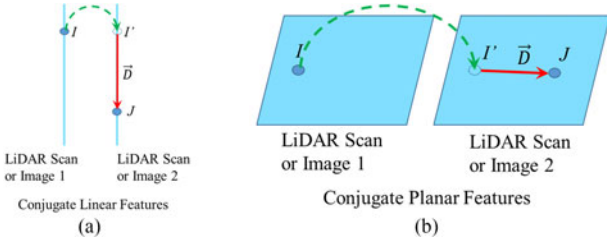
Fig. 7. Discrepancy vector between pseudo-conjugate points along corresponding (a) linear and (b) planar features.

pair, which nullifies the component of their discrepancy along the axial direction of the linear feature. This modified weight matrix is derived according to the estimated direction of the linear feature using the points from a reference LiDAR scan encompassing this feature [34]. The scan with the largest number of points belonging to a feature is set as the reference scan as it would result in the most reliable estimate of the feature direction. Note that an image can never be used as a reference since each feature point in an image has a different unknown scaling factor and so, they cannot be used to derive a reliable feature direction in object space. Hence, all the images and LiDAR scans are paired to a reference LiDAR scan, i.e., there would be no image-to-image pairings in the case of linear features.

In summary, if a linear feature is captured in n different LiDAR scans and m different images, then there will be a total of $(n-1)$ independent LiDAR-to-LiDAR pairings and m independent LiDAR-to-image pairings for each pseudo-conjugate point along the feature. A pseudo-conjugate LiDAR-to-LiDAR point pairing will give two equations and no unknowns, thus leading to a point definition redundancy of 2. Each pseudo-conjugate LiDAR-to-image point pairing will result in two equations and one unknown (scaling factor corresponding to the image point), i.e., the point definition redundancy is 1.

Planar-feature-based pairings: A planar feature is represented by a sequence of pseudo-conjugate points along the feature. Again, each pseudo-conjugate point pairing will result in a random misclosure vector ($\vec{e}$) along with a nonrandom misclosure vector ($\vec{D}$), as shown in Fig. 7(b) and stated before in (12). So, the discrepancy of the resultant point pair is minimized only along the direction normal to the planar surface, thus resulting in only one equation from each pseudo-conjugate point pair. Again, this is achieved by deriving a modified weight matrix using the normal direction of the planar surface based on the points from the corresponding reference LiDAR scan that encompass this feature [34]. This matrix would retain only the component of the discrepancy along the normal direction of the planar feature and nullify the other two. Similar to the discussion for linear features, an image cannot be used as reference for planar features as well. So, all the images and LiDAR scans will be paired to a reference LiDAR scan.

Let us consider a planar feature captured in n different LiDAR scans and m different images. Again, there will be a total of $(n-1)$ independent LiDAR-to-LiDAR pairings and m independent LiDAR-to-image pairings for each pseudo-conjugate point along the feature. A pseudo-conjugate LiDAR-to-LiDAR

point pairing will lead to one equation and no unknowns, which implies a point definition redundancy of 1. Each pseudo-conjugate LiDAR-to-image point pairing will result in one equation and one unknown (scaling factor corresponding to the image point), i.e., the point definition redundancy is 0. This implies that such pairings will not make a contribution toward the estimation of the calibration parameters. This leads to the conclusion that pseudo-conjugate image points from a planar feature cannot be used for calibration (as mentioned in Section II-D1). However, this model can be modified slightly by incorporating unique points belonging to a planar feature (such as the corners or center of a board) in different images. This would enable conjugate point pairings between different images for a planar feature. So, an image-to-image pairing for a point I belonging to a planar feature would result in three equations (and two unknowns) and a LiDAR-to-image pairing between one of the image points and a pseudo-conjugate LiDAR point will give an additional equation involving a scaling factor that has been already incorporated in the image-to-image point pairing. Hence, the point definition redundancy is increased to 2.

Based on this discussion, we can conclude that the following pairing scheme is optimal in order to conduct multi-LiDAR multicamera system calibration:

1) Image-to-image conjugate point pairing,
2) LiDAR-to-LiDAR and LiDAR-to-image pairings of pseudo-conjugate points belonging to corresponding linear features,
3) LiDAR-to-LiDAR pairings of pseudo-conjugate points along corresponding planar features, and
4) LiDAR-to-image pairings of pseudo-conjugate points belonging to corresponding planar features (which have distinct points that can be identified in images) along with image-to-image conjugate point pairs for the same feature.

E. Implementation of the Proposed Iterative Calibration Strategy

In this section, we summarize the proposed strategy to simultaneously calibrate the mounting parameters of several spinning multibeam laser scanners and cameras onboard a mobile platform using tie points and tie features (e.g., planar and linear features). After collecting data from several drive-runs/flight lines, a LiDAR-based 3-D point cloud relative to a global reference frame will be derived using the GNSS/INS-based position/orientation and initial estimates for the mounting parameters. Then, conjugate features are identified and extracted from the reconstructed point cloud. Similarly, images captured from different cameras and drive-runs/flight lines are used to measure the image coordinates of the points belonging to these conjugate features. The 3-D coordinates for the image points are computed using initial estimates of their scaling factors and camera mounting parameters along with the GNSS/INS position and orientation information.

The multi-LiDAR multicamera system calibration is based on minimizing the discrepancies among conjugate points, linear features, and/or planar features obtained from different laser

scanners, cameras, and/or drive-runs/flight lines. So, an optimal configuration should aim to maximize the impact of biases in calibration parameters so as to ensure an accurate estimation of the bias. So, the configuration used in a calibration mission is one where there are sufficient target primitives to establish a control in all three directions (along track, across track, and vertical directions). Moreover, the drive-run/flight-line configuration should include tracks in the same as well as opposite directions with different lateral separations between them. This research carries out an iterative calibration procedure where first, the discrepancy among extracted points/features is minimized using a modified weight matrix to derive mounting parameters through an LSA process. Then, the 3-D mapping frame coordinates for all the LiDAR and image points along the extracted features are recomputed using the newly estimated mounting parameters and scaling factors. The modified weight matrix is redefined depending on the newly obtained best-fitting line or plane from the reference LiDAR scan, and the discrepancy among conjugate features is minimized again using LSA with the newly defined modified weight matrix. The above-mentioned steps are repeated until the change in the estimates of the mounting parameters is below a predefined threshold.

The parameters that need to be estimated are the scaling factors for all the points measured in different images $(\lambda(i, Cj, t))$, the lever arm $(\Delta X, \Delta Y, \Delta Z)$, and boresight angles $(\Delta\omega, \Delta\phi, \Delta\kappa)$ for all the laser scanners and cameras. However, the vertical lever arm component ΔZ of the reference laser scanner is fixed during the calibration procedure as it cannot be estimated in the calibration procedure since any change in ΔZ will not introduce discrepancies among the different versions of the same feature captured from different laser scanners, cameras, and/or drive-runs/flight lines. It would only result in a shift of the point cloud in the vertical direction as a whole. So, it is either manually measured or determined using vertical control (such as horizontal planar patches with known elevation). The proposed methodology can incorporate ground control points, which can be paired to the corresponding image points or pseudo-conjugate LiDAR points along the corresponding feature. Moreover, ground control features can also be paired with LiDAR or image points belonging to the corresponding feature. One should note that due to the generic nature of the proposed calibration model, it is also capable of simultaneously estimating the intrinsic parameters of all the cameras as well as the laser scanners by using a sufficiently large number of conjugate point/feature pairs between different images/LiDAR scans captured from different drive-runs/flight lines. Now, we proceed to the evaluation of the proposed calibration technique using experimental results for different mobile mapping systems (airborne and terrestrial).

III. Experimental Results

In this research, three different mobile mapping platforms—a UAV-based system, a car-mount system, and a high clearance tractor (denoted henceforth as a PhenoRover-based system)—are used to collect LiDAR and photogrammetric data for 3-D
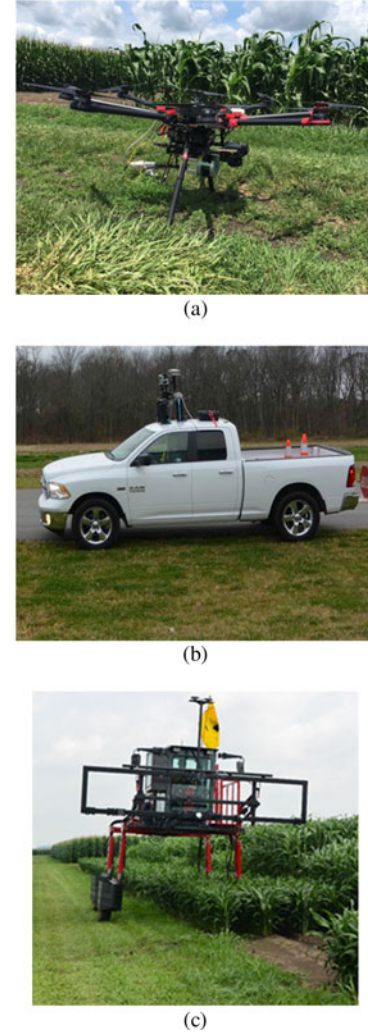

Fig. 8.   Mobile mapping systems. (a) UAV-based system. (b) Car-mount system. (c) PhenoRover-based system.

point cloud reconstruction, each of which is shown in Fig. 8(a), (b), and (c), respectively. The system specifications, dataset descriptions, and the calibration results for each of these systems are discussed in more detail in the forthcoming sections.

A. UAV-Based Mobile Mapping System (Single Laser Scanner and Single Camera)

The dataset used for evaluating the performance of the proposed calibration strategy for an airborne mobile mapping system was captured by a UAV-based system on a DJI M600 platform carrying a Velodyne VLP-16 laser scanner and a Sony Alpha 7R (ILCE-7R) camera, along with an APX-15 V2 as the GNSS/INS unit. A Raspberry Pi module is used to store the LiDAR data. The Velodyne VLP-16 has a typical range accuracy of 3 cm. The Sony Alpha 7R is a 36.4 MP off-the-shelf camera, which supports the goal of having the maximum image resolution to facilitate accurate orthophoto generation and 3-D point cloud reconstruction. In this research, the Applanix APX-15 V2 was chosen, considering its weight and accuracy. For this unit, the postprocessing accuracy in position is 2–5 cm and the predicted accuracy for the roll/pitch and heading is
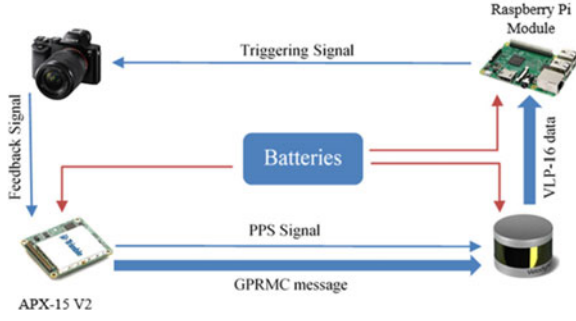
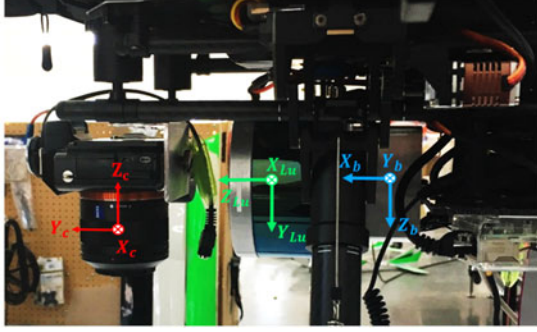Fig. 9. Integration scheme for the M600 UAV-based system.

Fig. 10. UAV-based MMS and the involved coordinate systems.

0.025 and 0.08°, respectively [35]. These values were used to compute the expected achievable accuracy for the computed mapping frame coordinates using the LiDAR error propagation calculator developed by [36]. The calculator suggests that for a flying height of 20 m (used in this experiment), we should expect an accuracy of around 5–6 cm for the derived point cloud coordinates. Similarly, an error propagation for image-based 3-D point positioning is also conducted while considering the accuracy of the GNSS/INS position/orientation information along with the error in image coordinate measurement (∼2 pixels), pixel size (4.86 μm), the accuracy of estimation of mounting parameters, and the intersection accuracy according to the overlap between successive images (∼70%). The results indicate an expected accuracy of 6 cm for a flying height of 20 m in case of image-based 3-D point positioning. The block diagram of the M600 UAV-based MMS indicating triggering signals, feedback signals, and communication wires/ports between sensors and power connections is shown in Fig. 9.

The setup for the UAV-based MMS and the coordinate systems for the laser unit, camera, and the IMU body frame are shown in Fig. 10. One should note that the rotation between the laser unit and the IMU body frame coordinate systems (R_{Lu}^{b}) for this system involves a secondary rotation of 90°, which would cause a gimbal lock problem [37]. In order to avoid this gimbal lock problem, we introduce a virtual LiDAR unit frame (Lu') that is approximately aligned with the IMU body frame. So, the mounting parameters relating the virtual LiDAR unit frame and the IMU body frame $(r_{Lu'}^{b}$ and $R_{Lu'}^{b})$ are estimated during calibration, while a fixed rotation $(R_{Lu}^{Lu'})$ relates the actual LiDAR unit frame to the former.

The dataset collected by the UAV-based system covers 16 specially designed highly reflective boards (75 cm wide stop signs, 90 cm × 60 cm wrong way signs, and 60 cm × 60 cm checkerboard targets) that can be easily identified as high-intensity regions in the airborne LiDAR data, and each of their corners can be distinctly identified and paired in different images. Five hut-shaped target boards (with two 60 cm × 120 cm planar boards) are also deployed, with their ridges oriented perpendicular to each other. The two surfaces corresponding to each of these huts are used as planar features for calibration, and their ridges are used as conjugate linear features between the images and the overlapping LiDAR point clouds from different flight lines. Note that the two planar features of hut-shaped targets are indeed not independent of their derived linear feature. However, the aim of this paper is to demonstrate the accuracy of the proposed calibration strategy, and in this regard, the correlation between these features is ignored and the planar as well as linear features of the hut-shaped targets can be used for calibration with their RMSEs indicating the quality of calibration. Four planar rooftops of a shed covered by the flight lines are also used as planar features. All these features ensure enough control along the *X*-, *Y*-, and *Z*-directions. In this experiment, the flight path of the UAV comprises ten flight lines at a fixed height of 20 m above the ground, with different directions and lateral distances between them. The flight lines cover the calibration primitives at an approximate speed of 1.5 miles/h. The camera is set to capture images at an interval of 1.5 s. Fig. 11(a) shows a portion of the calibration test field with the calibration primitives circled in red, and Fig. 11(b) shows the configuration of flight lines and target primitives, where PB denotes the used planar boards, PV denotes the planar hut surfaces or rooftops, and LH denotes the linear hut ridges. With ten flight lines and one laser unit, we will have a total of ten versions for each of the features used for the calibration procedure from the LiDAR-based point cloud. Similarly, the coordinate measurements from each image can be paired to a reference image in case of conjugate points or the reference version from LiDAR (i.e., the one consisting of most points along that feature) in the case of pseudo-conjugate points along a feature. A total of 155 images were used to measure the image coordinates for various calibration primitives, where each target primitive was observed in ∼15–20 images captured in different flight lines. Finally, the proposed calibration procedure was applied to obtain the mounting parameters for both the laser scanner and the camera simultaneously.

A qualitative evaluation of the calibration results is done in two different ways:

1) checking the alignment in object space by computing the 3-D mapping frame coordinates for all the LiDAR and image points using the GNSS/INS position and orientation information, the estimated mounting parameters for the sensors, and the estimated scaling factors for the image points; and
2) checking the alignment in image space by evaluating the pixel coordinates for all the LiDAR and image points based on their 3-D mapping frame coordinates after calibration.
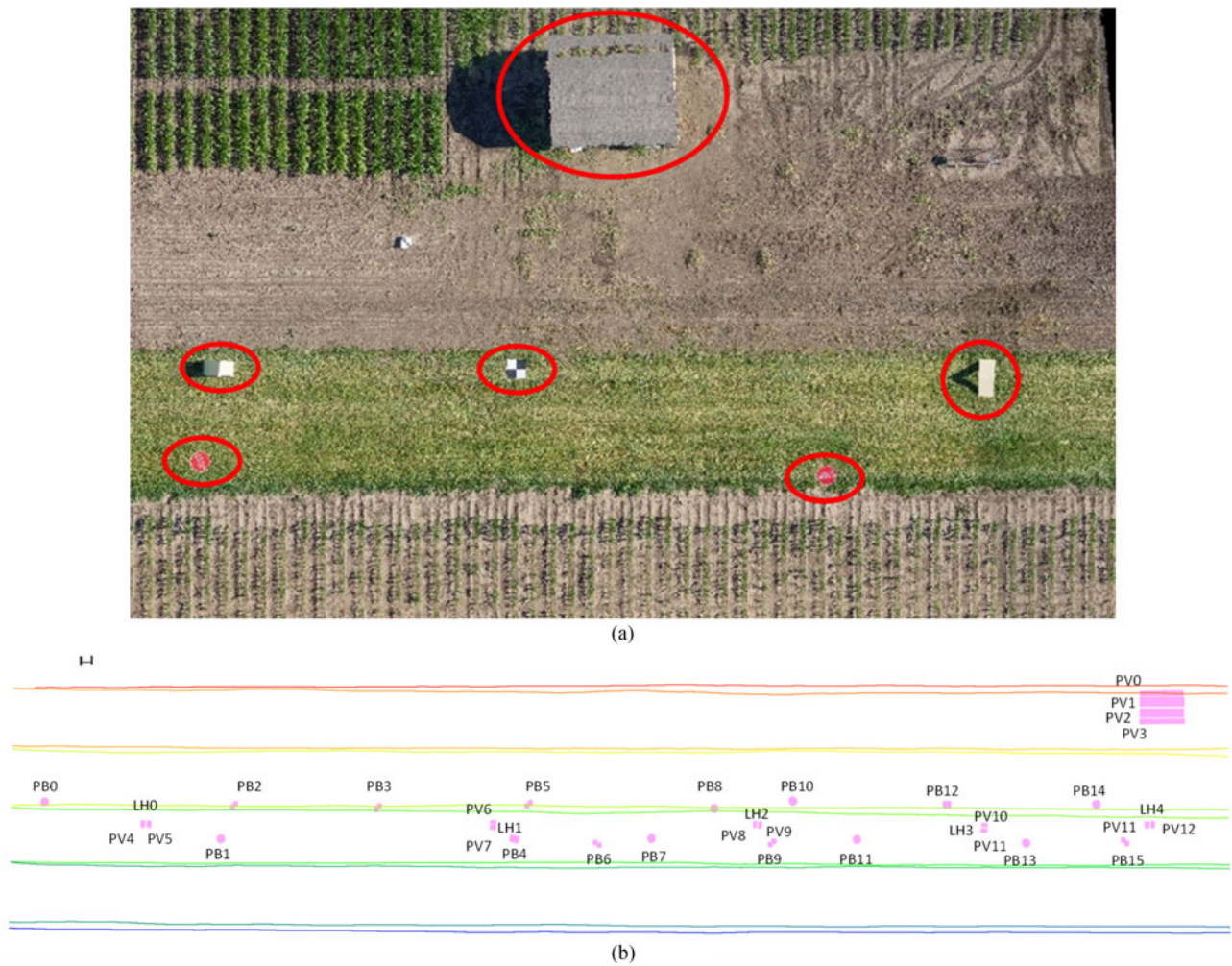
Fig. 11.   UAV-based system. (a) Calibration test field. (b) Configuration of flight lines and calibration primitives.
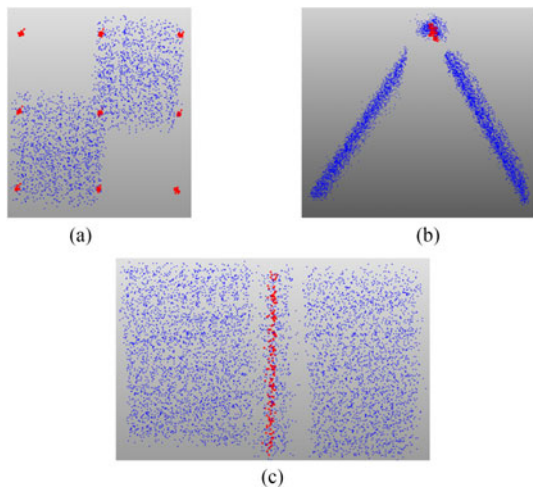

Fig. 12.   Qualitative evaluation of 3-D alignment between LiDAR (blue) and image-based object points (red) after calibration. (a) Specially designed checkerboard target and its corners. (b) Front view of the hut-shaped target. (c) Top view of the same hut-shaped target.

Fig. 12 shows the LiDAR and image points (in blue and red, respectively) for a checkerboard target and a hut-shaped target in the object space after calibration. From that figure, one can see that the corners of the checkerboard target measured in different images align well with the high-intensity LiDAR points. Similarly, the image points along the hut ridge are aligned in 3D with the corresponding LiDAR points. Fig. 13 shows the alignment of LiDAR and image points in image space by assigning blue color to the pixels corresponding to the LiDAR feature points and red color to those corresponding to the object points derived from image measurements and the estimated calibration parameters.

The initial approximations of all the mounting parameters and the final results (along with their standard deviations) after calibration are listed in Table I, where the parameters highlighted in red are fixed during calibration. One should note that apart from the vertical lever arm component (ΔZ) of the laser scanner, the planimetric lever arm components (ΔX, ΔY) are also fixed (obtained from manual measurements). Only the vertical lever arm component (ΔZ) of the camera and the boresight parameters ($\Delta \omega, \Delta \phi, \Delta \kappa$) for the laser scanner and camera are estimated. This is due to the fact that all the flight lines used for calibration are at the same flying height, and according to the previous work by Habib *et al.* [38], different flying heights are required in order to eliminate the correlation between the plani-
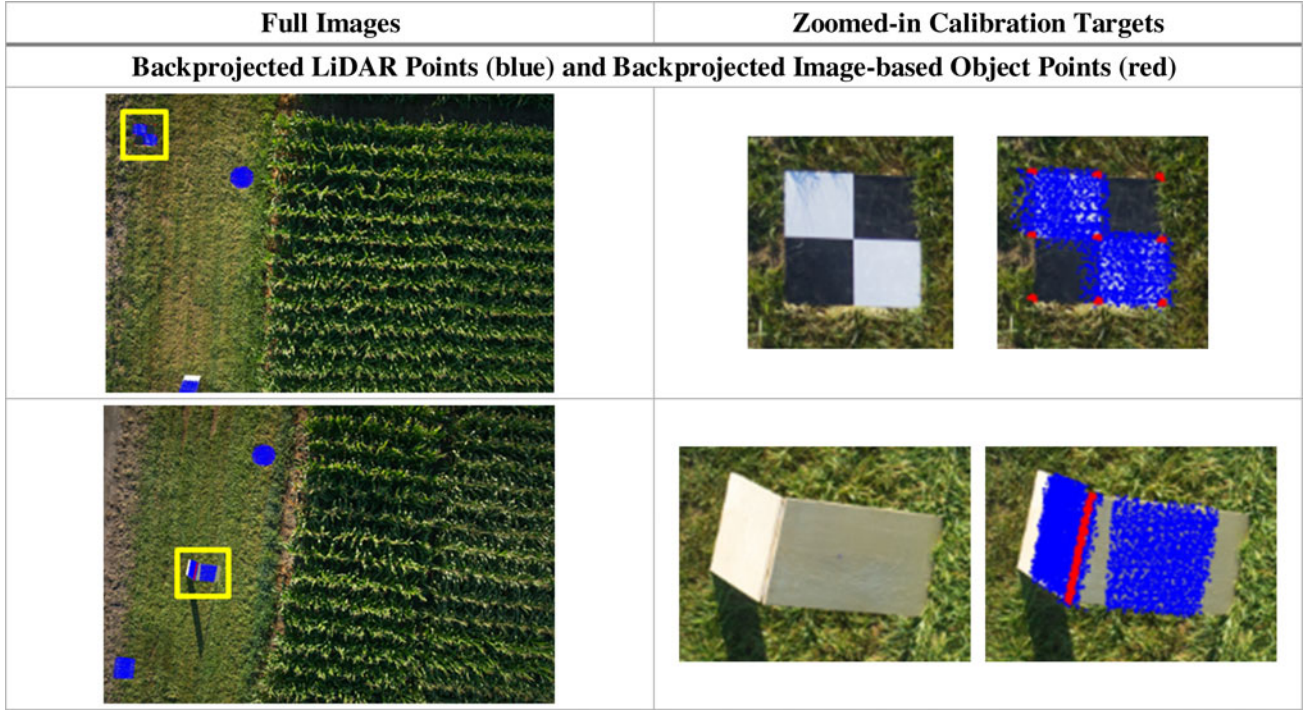
Fig. 13. Qualitative evaluation of 2-D alignment between LiDAR data and image-based object points by projecting them onto the image space after calibration.

TABLE I
MOUNTING PARAMETERS BEFORE AND AFTER CALIBRATION OF THE UAV-BASED SYSTEM

VLP-16 LiDAR Unit Mounting Parameters $(r_{Lu'}^b)$ $(R_{Lu'}^b)$						
	ΔX (m)	ΔY (m)	ΔZ (m)	$\Delta\omega$ (°)	$\Delta\phi$ (°)	$\Delta\kappa$ (°)
Initial	0.020	0	0	0	0	0
Final	0.020	0	0	0.1898	0.3008	-0.0950
Standard Deviation	Fixed	Fixed	Fixed	0.0165	0.0209	0.0340
Sony α7R Camera Mounting Parameters (r_C^b) (R_C^b)						
	ΔX (m)	ΔY (m)	ΔZ (m)	$\Delta\omega$ (°)	$\Delta\phi$ (°)	$\Delta\kappa$ (°)
Initial	0.130	-0.040	0.05	180	0	-90
Final	0.130	-0.040	0.0271	179.7720	-0.2339	-90.4132
Standard Deviation	Fixed	Fixed	0.0522	0.0389	0.0389	0.0733

metric lever-arm components and the boresight angles. Here, the lever arm components are measured to an accuracy of about 1 cm. One should note that any loss of accuracy in the planimetric lever-arm components would be accounted for in the boresight angles estimation, thus preventing any loss of accuracy in point positioning after calibration due to slightly inaccurate manual measurements. The proposed calibration strategy is capable of estimating the intrinsic camera parameters (e.g., the location of principal point and the principal distance), but according to [39], these can be estimated along with the mounting parameters only if images captured from different heights are available. The square root of the *a posteriori* variance factor

$(\hat{\sigma}_o)$ represents the average compatibility between all the conjugate and pseudo-conjugate point pairings, which is 2.07 cm after calibration in this case. This is better than the expected accuracy of around 5–6 cm for a flying height of 20 m according to the accuracies of the hardware involved. For quantitative evaluation, first, the object points derived from LiDAR unit and camera are considered together for computing the RMSE for all the features. Then, the object points derived from each sensor are considered separately to compute the RMSE of normal distance for each feature using the corresponding line/plane parameters derived as a result of combined calibration. Note that the RMSE for some features are marked as NA in case of just the camera being considered individually because there are no image points observed for the corresponding feature. The RMSE of normal distance of LiDAR and image-based object points from best-fitting plane/line for extracted features before and after calibration for combined sensors as well as individual LiDAR unit and camera are listed in Table II. Here, the points used to evaluate the RMSE are actually the ones that were used to determine the mounting parameters. So, these RMSE values computed for the fitting residuals for all the features indicate the internal accuracy of calibration.

B. Car-Mount Mobile Mapping System (Two Laser Scanners and Single Camera)

Unlike the UAV-based MMS, the car-mount system has no payload restrictions, such as sensor weight, size, or power consumption. This enables the installation of a larger and more accurate GNSS/INS unit. Moreover, a computer is used instead of the Raspberry Pi to store the LiDAR and image data, which in turn allows longer missions. This system consists of two

TABLE II
CALIBRATION OF THE UAV-BASED SYSTEM: SQUARE ROOT OF THE *A Posteriori* VARIANCE FACTOR $(\hat{\sigma}_o)$ AND RMSE OF PLANE/LINE FITTING

|	Number of LiDAR Points	Number of Image Points	Before Calibration	After Calibration $(\boldsymbol{Lu}, \boldsymbol{C})$	After calibration $(\boldsymbol{Lu})$	After calibration $(\boldsymbol{C})$
Feature ID					RMSE (m)	
Reflective Boards						
Board 0	4,377	145	0.040	0.021	0.021	
Board 1	4,610	155	0.037	0.019	0.019	
Board 2	2,521	157	0.036	0.019	0.019	
Board 3	2,465	168	0.037	0.020	0.020	
Board 4	5,276	142	0.040	0.023	0.023	
Board 5	2,462	162	0.039	0.023	0.023	
Board 6	2,184	168	0.036	0.022	0.022	
Board 7	4,654	150	0.036	0.019	0.019	
Board 8	4,418	144	0.034	0.018	0.018	Avg. RMSE for point-based adjustment = 0.009
Board 9	2,402	171	0.034	0.020	0.020	
Board 10	4,595	143	0.039	0.026	0.026	
Board 11	4,712	149	0.034	0.022	0.022	
Board 12	4,710	147	0.036	0.023	0.023	
Board 13	4,386	151	0.033	0.024	0.024	
Board 14	4,220	148	0.034	0.021	0.021	
Board 15	2,476	165	0.035	0.021	0.021	
Planar Shed Rooftops						
Rooftop 0	13,115	0	0.056	0.024	0.024	
Rooftop 1	38,495	0	0.047	0.034	0.034	NA
Rooftop 2	40,739	0	0.028	0.026	0.026	
Rooftop 3	21,577	0	0.039	0.025	0.025	
Hut Ridges						
Ridge 0	732	172	0.107	0.018	0.019	0.010
Ridge 1	520	195	0.096	0.017	0.017	0.018
Ridge 2	647	168	0.111	0.014	0.015	0.012
Ridge 3	627	186	0.122	0.018	0.018	0.017
Ridge 4	785	182	0.114	0.018	0.019	0.015
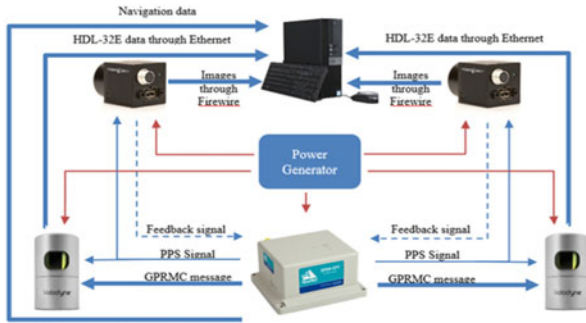
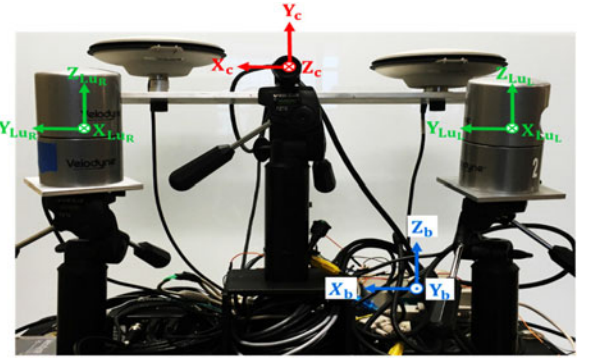Fig. 14.   Integration scheme for the car-mount mobile mapping system.

Fig. 15.   Car-mount MMS and the involved coordinate systems.

Velodyne HDL-32E laser scanners and an FLIR Flea-2G camera, which are directly georeferenced by a Novatel SPAN-CPT unit. The Velodyne HDL-32E has a typical range accuracy of 2 cm. The FLIR Flea-2G camera has a maximum image resolution of 5 MP and has built-in ports for both triggering and strobe feedback signals. For the SPAN-CPT, the postprocessing accuracy in position can be less than 2 cm and the estimated accuracy for the roll/pitch and heading are 0.015° and 0.08°, respectively [40]. These values were used to evaluate the expected accuracy in the derived mapping frame coordinates for the individual points using the LiDAR error propagation calculator developed by Habib *et al.* [36]. The calculator suggests that we should expect an accuracy of around 3 cm for the derived

point cloud coordinates at a range of 30 m. Based on the focal length (12 mm), pixel size (3.45 μm), an error of $\sim$2 pixels in image coordinate measurement, the accuracy of GNSS/INS position/orientation and mounting parameters, and the intersection accuracy according to the overlap between successive images ($\sim$80%), an error propagation for image-based 3-D point positioning indicates an expected accuracy in a range of $\sim$2–20 cm for objects at 5–100 m from the camera, respectively. The block diagram for this system, illustrating triggering signals, feedback signals, and communication wires/ports between sensors and power connections are shown in Fig. 14. The setup for the
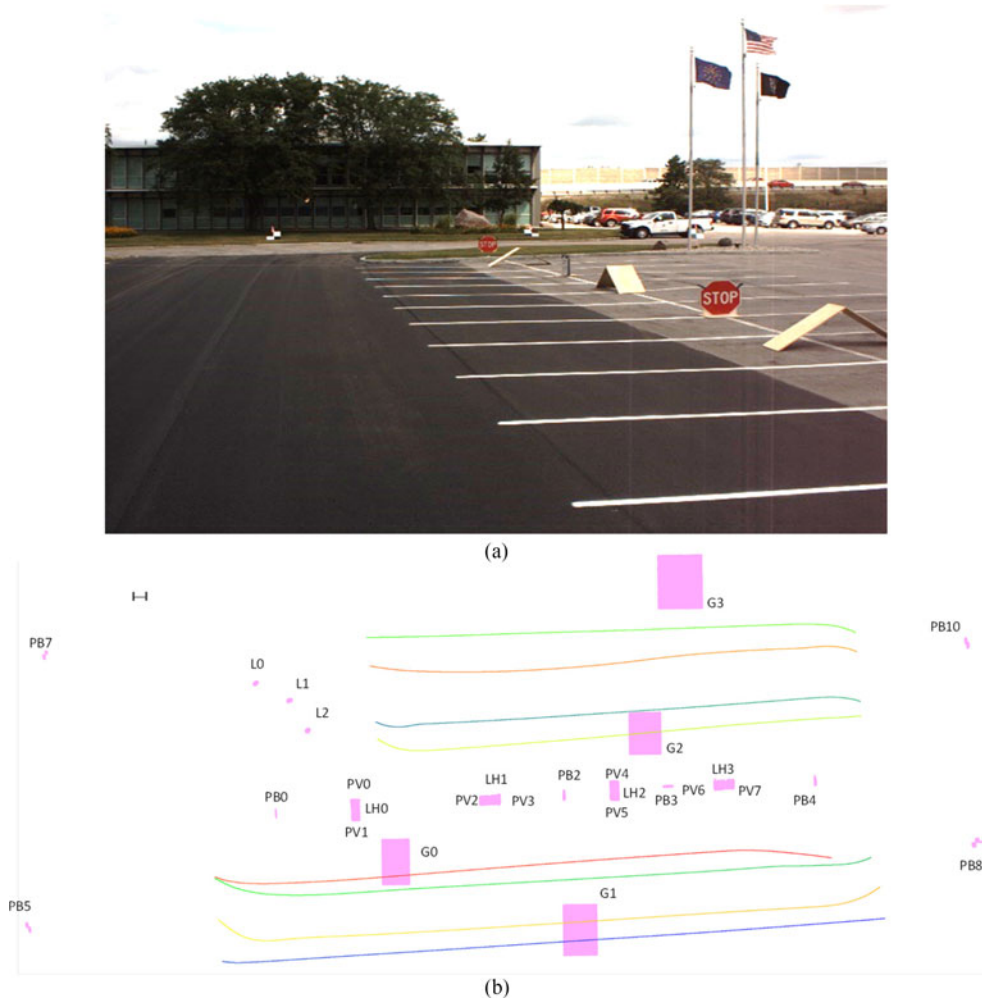
Fig. 16. Car-mount system. (a) Calibration test field. (b) Configuration of drive runs and calibration primitives.
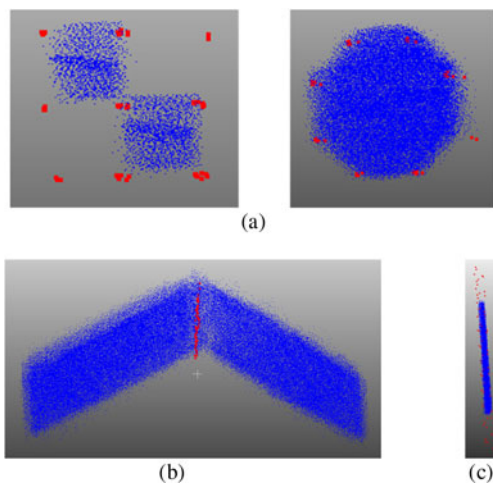

Fig. 17. Qualitative evaluation of 3-D alignment between LiDAR (blue) and image-based object points (red) after calibration. (a) Specially designed boards and their corners. (b) Hut-shaped target. (c) Flag pole.

car-mount system and the coordinate systems for the laser units, camera, and the IMU body frame are shown in Fig. 15.

The targets deployed for the UAV-based system calibration (specially designed boards and hut-shaped targets) were deployed again for the calibration of the car-mount system. However, instead of the boards being horizontal, they are vertical and perpendicular to each other. The boards and huts, along with some ground patches and flag poles, ensure enough control along the X-, Y-, Z-directions. In this experiment, eight drive runs having a length of approximately 40 m each, with different directions and lateral distance between them, were made around the calibration primitives at an approximate speed of 4 miles/h. The camera is set to capture images at an interval of 1 s. With eight drive runs and two laser units, we will have a total of 16 versions for each of the features used for the calibration procedure. A total of 45 images were used to measure the image coordinates for the different calibration primitives. Fig. 16(a) shows the calibration test field, and Fig. 16(b) shows the configuration of drive runs and target primitives, where PB denotes highly reflective planar boards, PV denotes the planar hut surfaces, G denotes ground patches, L denotes light poles, and LH denotes linear hut ridges. For the car-mount system, one of the HDL-32E scanners is taken as reference and the other is considered a slave unit. The proposed calibration procedure is applied to obtain the

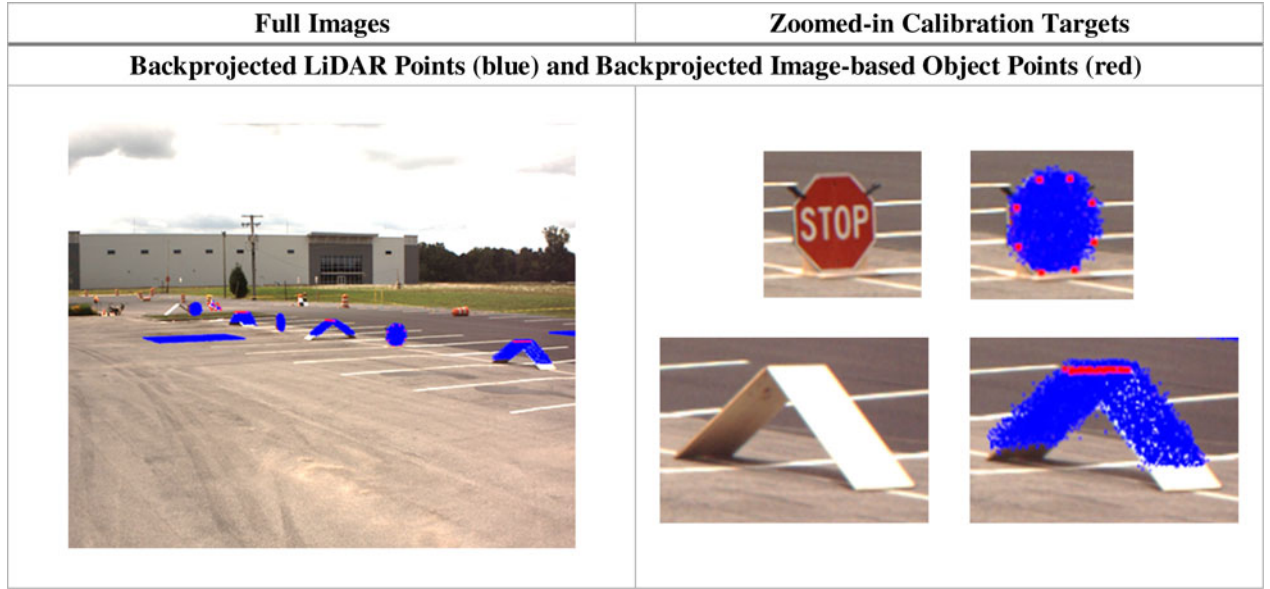| Full Images	Zoomed-in Calibration Targets
Backprojected LiDAR Points (blue) and Backprojected Image-based Object Points (red)	

Fig. 18. Qualitative evaluation of 2-D alignment between LiDAR data and images after calibration for the car-mount system.

TABLE III
MOUNTING PARAMETERS BEFORE AND AFTER CALIBRATION OF THE CAR-MOUNT SYSTEM

	ΔX (m)	ΔY (m)	ΔZ (m)	Δω (°)	Δφ (°)	Δκ (°)
Reference Unit: HDL-32E (Left) LiDAR Unit Mounting Parameters $\left(r_{Lu_L}^b\right)\left(R_{Lu_L}^b\right)$						
Initial	0	0.20	0.32	−5	0	−60
Final	-0.0140	0.1994	0.32	-6.4629	1.2256	-66.0297
Std. Dev.	0.0056	0.0054	Fixed	0.0094	0.0105	0.0127
HDL-32E (Right) LiDAR Unit Mounting Parameters $\left(r_{Lu_R}^{Lu_L}\right)\left(R_{Lu_R}^{Lu_L}\right)$						
Initial	0.25	0.43	0	0	0	0
Final	0.1849	0.4659	0.0112	0.7595	0.2802	12.5389
Std. Dev.	0.0070	0.0068	0.0043	0.0121	0.0103	0.0154
Flea-2G Camera Mounting Parameters $\left(r_{c}^b\right)\left(R_{c}^b\right)$						
Initial	0.270	0.190	0.328	90	−5	0
Final	0.270	0.190	0.3132	92.0029	−5.2838	−1.5348
Std. Dev.	Fixed	Fixed	0.0381	0.0418	0.0343	0.0650

mounting parameters for the two laser scanners and the camera simultaneously, using the features extracted from LiDAR point clouds and the distortion-free image coordinates.

In this case, apart from the lever arm ΔZ for the reference sensor, the lever arm parameters $(\Delta X, \Delta Y)$ for the camera are also fixed during the calibration procedure as they are highly correlated with the boresight angles of the camera because of the narrow angular field of the view of the Flea-2G camera. Figs. 17 and 18 depict the qualitative evaluation of the calibration by showing the alignment of LiDAR and image-based object points belonging to different features in the mapping space (3D) and image space (2D), respectively. The initial approximations and the final results (along with their standard deviations) of all the mounting parameters are listed in Table III, where the parameters fixed during calibration are highlighted in red. The square root of the *a posteriori* variance factor $(\hat{\sigma}_o)$ after calibration is 1.73 cm in this case. This is better than the expected accuracy of around 3 cm according to the accuracies

of the hardware involved. Similar to a UAV-based system, the RMSE of normal distance of LiDAR and image-based object points from best-fitting plane/line for extracted features before and after calibration for combined sensors as well as individual LiDAR units and camera are listed in Table IV, which indicates the validity of the proposed system calibration procedure. Again, the RMSE for some features is marked as NA in case of just the camera being considered individually because there are no image points observed for the corresponding feature. Note that the proposed calibration approach is dependent on the extracted features, so it is imperative to evaluate the effect of feature extraction accuracy on the calibration results. The final RMSE of a feature obtained after calibration would reflect the feature extraction accuracy along with the calibration accuracy. If the accuracy of feature extraction is low (i.e., the final RMSE is high), then the reliability of calibration results would decrease and it would be recommended to conduct a more accurate extraction of the feature and recalibrate the sys-

TABLE IV
CALIBRATION OF THE CAR-MOUNT SYSTEM: SQUARE ROOT OF THE *A Posteriori* VARIANCE FACTOR $(\hat{\sigma}_o)$ AND RMSE OF PLANE/LINE FITTING THROUGH THE DIFFERENT ITERATIONS

	Number of LiDAR Points	Number of Image Points	Before Calibration	After Calibration (Lu_L, Lu_R, C)	After Calibration (Lu_L)	After Calibration (Lu_R)	After Calibration (C)
Feature ID				**RMSE (m)**			
Reflective Boards							
Board 0	20,184	56	0.414	0.020	0.021	0.018	Avg. RMSE for point-based adjustment = 0.011
Board 1	78,007	56	0.365	0.028	0.025	0.031	
Board 2	105,227	93	0.301	0.028	0.026	0.030	
Board 3	47,266	57	0.405	0.030	0.028	0.031	
Board 4	958	64	0.149	0.013	0.014	0.012	
Board 5	582	82	0.210	0.016	0.013	0.020	
Board 6	4,378	88	0.246	0.020	0.019	0.022	
Board 7	10,397	67	0.407	0.017	0.016	0.019	
Ground Patches							
Ground 0	802,878	0	0.204	0.016	0.016	0.016	NA
Ground 1	956,653	0	0.210	0.014	0.014	0.015	
Ground 2	988,163	0	0.229	0.016	0.017	0.016	
Ground 3	1,209,071	0	0.205	0.016	0.015	0.017	
Hut Ridges							
Ridge 0	3,775	18	0.238	0.020	0.017	0.022	0.023
Ridge 1	5,308	64	0.290	0.019	0.017	0.020	0.021
Ridge 2	7,660	37	0.525	0.018	0.017	0.020	0.024
Ridge 3	4,498	65	0.285	0.018	0.018	0.017	0.020
Flag Poles							
Pole 0	41,810	64	0.934	0.032	0.034	0.031	0.035
Pole 1	33,929	66	0.934	0.033	0.036	0.030	0.038
Pole 2	39,361	66	0.894	0.031	0.036	0.028	0.037

tem. Also, the buffer used for extraction of various features is set according to the accuracy of initial estimates of calibration parameters.

C. PhenoRover-Based Mobile Mapping System (Two Laser Scanners and Two Cameras)

The mobile mapping system onboard the PhenoRover consists of two Velodyne HDL-32E laser scanners and two FLIR Flea-2G cameras, which are directly georeferenced by an Applanix POSLV-125 unit. Both cameras capture images at a rate of 1 frame per second, thus leading to a stereo pair of images every second. For the POSLV-125, the postprocessing accuracy in position can be 2–5 cm and the estimated accuracy for the roll/pitch and heading can be 0.025° and 0.06°, respectively [41]. These values were used to evaluate the expected accuracy of the derived mapping frame coordinates using the LiDAR error propagation calculator developed by Habib *et al.* [36]. The calculator indicates that we should expect an accuracy of around 5 cm at a range of 30 m. Based on the focal length (12 mm), pixel size (3.45 μm), an error of ~2 pixels in image coordinate measurement, the accuracy of GNSS/INS position/orientation and mounting parameters, and the height-to-base ratio (~4.5), an error propagation for image-based 3-D point positioning indicates an expected accuracy of 5 cm for images captured from a height of ~5 m. The setup for the PhenoRover-based MMS and the coordinate systems for the laser units, cameras, and the IMU body frame are shown in Fig. 19. Here, it should be noted that the rotations between each laser unit and the IMU body frame coordinate systems $(R_{Lu_L}^b$ and $R_{Lu_R}^b)$ involve a
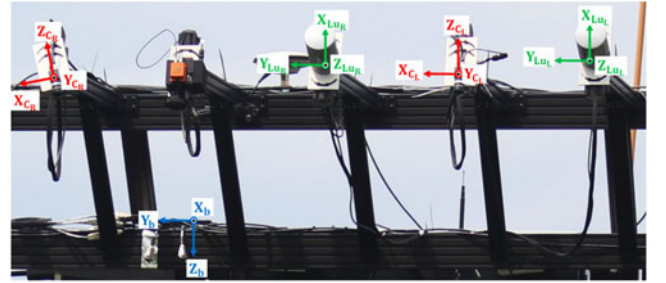

Fig. 19. PhenoRover-based MMS and the involved coordinate systems.

secondary rotation of 90°, which would cause a gimbal lock problem. In order to avoid this gimbal lock problem, we introduce a virtual LiDAR unit frame corresponding to each laser unit $(Lu_L'$ and $Lu_R')$ that is approximately parallel to the IMU body frame. So, the mounting parameters relating the virtual reference LiDAR unit frame (here, Lu_L') to the IMU body frame $(r_{Lu_L'}^b$ and $R_{Lu_L'}^b)$ and the transformations relating the two virtual LiDAR unit frames $(r_{Lu_R'}^{Lu_L'}$ and $R_{Lu_R'}^{Lu_L'})$ are estimated during calibration, while fixed rotations $(R_{Lu_L}^{Lu_L'}$ and $R_{Lu_R}^{Lu_R'})$ relate the virtual to the actual LiDAR unit frame for the respective laser units.

The setup of calibration primitives is similar to the one used for the car-mount system. In this experiment, ten drive runs, with different directions and lateral distances between them, were made around the calibration primitives at an approximate speed of 1.5 miles/h. A total of 132 images from both cam-
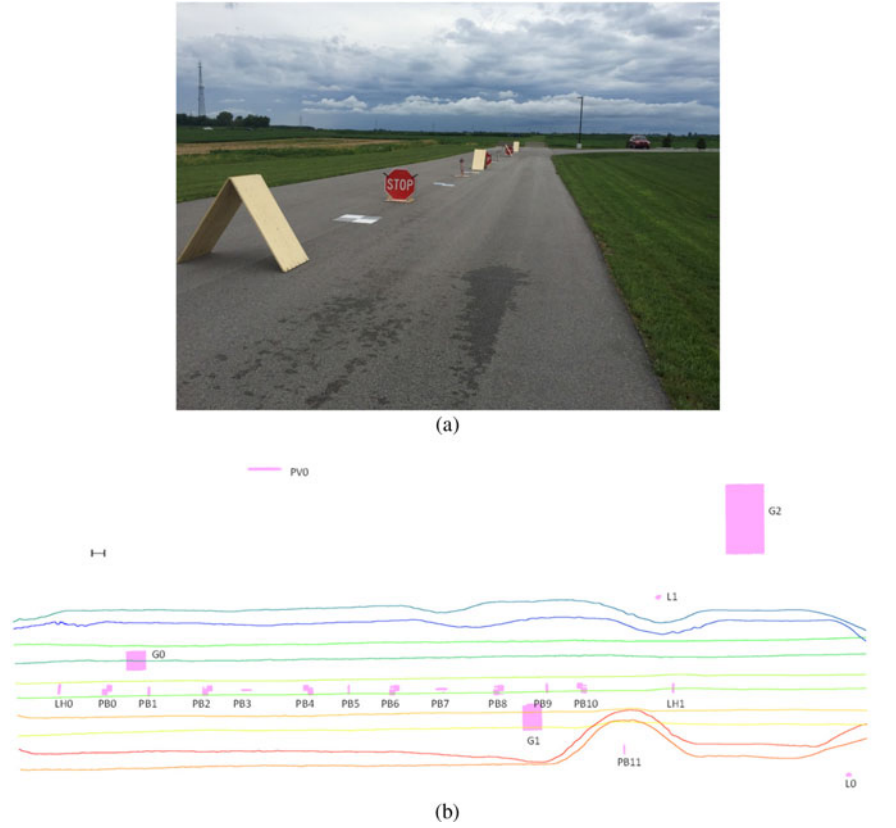
Fig. 20. PhenoRover-based system. (a) Calibration test field. (b) Configuration of drive runs and calibration primitives.

eras captured in two opposite drive-runs were used to measure the image coordinates for the different calibration targets, where each target primitive was observed in about 15 images. Fig. 20(a) shows the calibration test field, and Fig. 20(b) shows the configuration of drive-runs and boards, where PB denotes highly reflective planar boards, G denotes ground patches, L denotes light poles, and LH denotes linear hut ridges. The proposed multiLiDAR unit calibration procedure is applied to obtain the mounting parameters for both laser units and both cameras simultaneously.

For this system, apart from the vertical lever arm component (ΔZ) for the reference laser unit, the planimetric lever arm components $(\Delta X, \Delta Y)$ for the cameras are also fixed during the calibration procedure as they are highly correlated with the boresight angles of the cameras. The planimetric lever-arm components relating the reference camera to the IMU body frame are obtained from manual measurements, whereas the ones relating the slave camera to the reference camera are derived from an indoor stereo-camera calibration. Figs. 21 and 22 depict the qualitative evaluation of the calibration by showing the alignment of LiDAR and image points belonging to different features in the mapping space (3D) and image space (2D), respectively. The initial approximations and the final results (along with their standard deviations) of all the mounting parameters are listed in Table V, where the parameters fixed during calibration are highlighted in red. The initial estimates of the mounting parameters relating the reference and slave cameras are set to the values from indoor stereo-camera calibration and it should be noted that
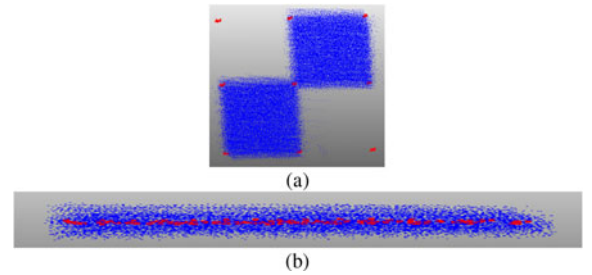

Fig. 21. Qualitative evaluation of 3-D alignment between LiDAR (blue) and image-based object points (red) after calibration. (a) Checkerboard target and its corners. (b) Ridge of the hut-shaped target.

the parameters obtained from the proposed calibration strategy closely match the results from indoor calibration. The square root of the *a posteriori* variance factor $(\hat{\sigma}_o)$ after calibration is 1.73 cm in this case. This is better than the expected accuracy of around 5 cm for a range of 30 m according to the accuracies of the hardware involved. The RMSE of normal distance of LiDAR and image-based object points from best-fitting plane/line for extracted features before and after calibration for combined sensors as well as individual LiDAR units and cameras are listed in Table VI, which indicate a significant improvement in the alignment of the features. Again, the RMSE for some features is marked as NA in case of just the cameras being considered individually because there are no image points observed for the corresponding feature. Note that there are no image points for some linear features (such as light poles) since the cameras
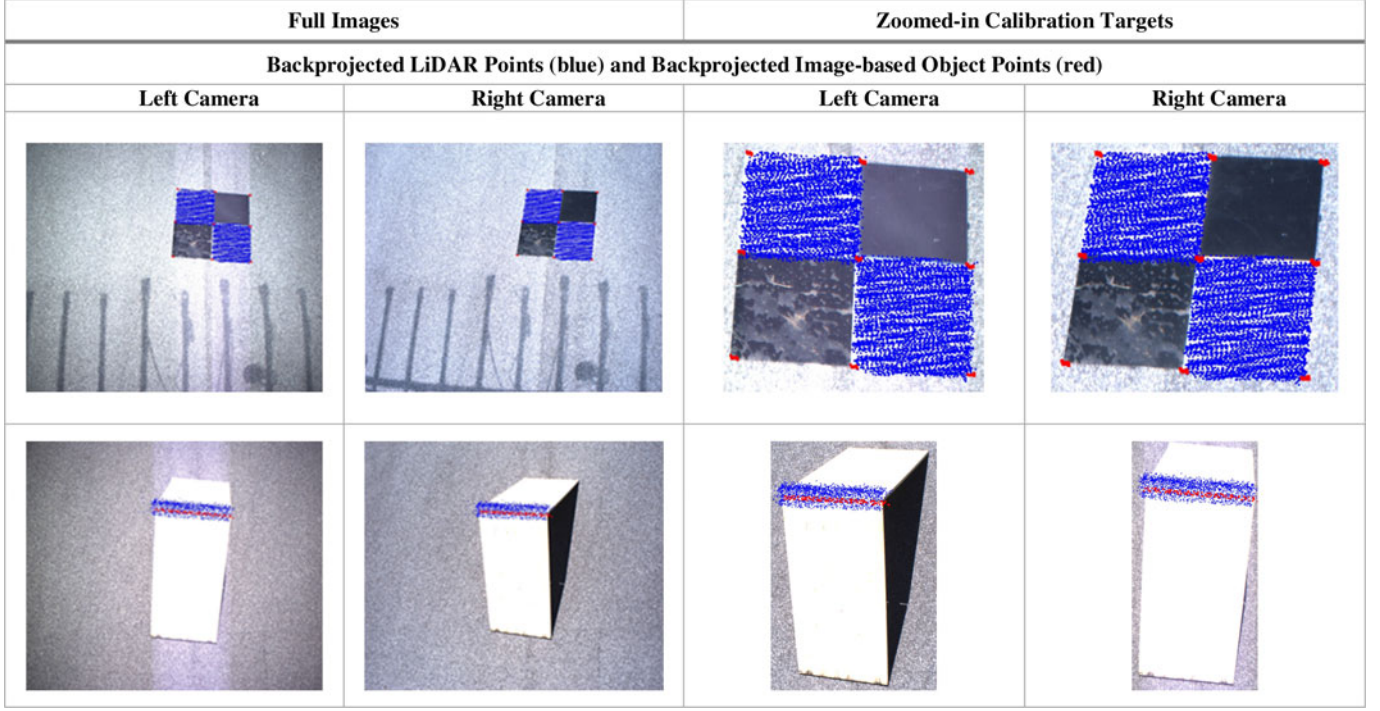
Fig. 22. Stereo-pair images for qualitative evaluation of 2-D alignment between LiDAR data and images after calibration for the PhenoRover-based system.

TABLE V
MOUNTING PARAMETERS BEFORE AND AFTER CALIBRATION OF THE PHENOROVER-BASED SYSTEM

	ΔX (m)	ΔY (m)	ΔZ (m)	Δω (°)	Δφ (°)	Δκ (°)
Reference Unit: HDL-32E (Left) LiDAR Unit Mounting Parameters $\left(r^{b}_{Lu'_{L}}\right)\left(R^{b}_{Lu'_{L}}\right)$						
Initial	1.30	-1.30	-0.41	0	15	0
Final	1.3819	-1.3560	-0.41	0.7194	17.3807	-0.6817
Standard Deviation	0.0091	0.0062	Fixed	0.0149	0.0205	0.0266
HDL-32E (Right) LiDAR Unit Mounting Parameters $\left(r^{Lu'_{L}}_{Lu'_{R}}\right)\left(R^{Lu'_{L}}_{Lu'_{R}}\right)$						
Initial	0	0.80	0	0	0	0
Final	-0.0102	0.7453	-0.0221	-1.1590	6.2276	-0.2605
Standard Deviation	0.0096	0.0068	0.0052	0.0187	0.0222	0.0288
Reference Camera: Flea-2G (Left) Camera Mounting Parameters $\left(r^{b}_{C_{L}}\right)\left(R^{b}_{C_{L}}\right)$						
Initial	1.35	-0.95	-0.28	180	0	-90
Final	1.35	-0.95	-0.2809	180.2630	-25.0466	-90.1679
Standard Deviation	Fixed	Fixed	0.0621	0.0917	0.0921	0.1411
Flea-2G (Right) Camera Mounting Parameters $\left(r^{C_{L}}_{C_{R}}\right)\left(R^{C_{L}}_{C_{R}}\right)$						
Initial	1.1248	0.0051	-0.0054	-0.3582	16.6633	-0.4590
Final	1.1248	0.0051	-0.0053	-0.3582	16.6633	-0.4590
Standard Deviation	Fixed	Fixed	0.0647	0.0930	0.0931	0.1407

are both looking downward, and hence, these features are not captured in any of the images.

IV. CONCLUSION AND RECOMMENDATIONS FOR FUTURE RESEARCH

In this paper, we proposed a point-pairing-based calibration strategy for multi-LiDAR multicamera mobile mapping systems,a which can derive the mounting parameters of multiple laser units and cameras simultaneously for airborne as well as terrestrial mobile mapping systems. This avoids the need to perform a separate calibration for each laser unit and each camera. The point-pairing-based bundle adjustment was theoretically compared with the conventional bundle adjustment, which revealed the equivalency of the two models in terms of their parameter estimation ability. The proposed calibration procedure can utilize different types of conjugate features (i.e., planar, linear) from the LiDAR data, along with conjugate or pseudo-conjugate

TABLE VI
CALIBRATION OF THE PHENOROVER-BASED SYSTEM: SQUARE ROOT OF THE *A Posteriori* VARIANCE FACTOR ($\hat{\sigma}_o$) AND RMSE OF PLANE/LINE FITTING

	Number of LiDAR Points	Number of Image Points	Before Calibration	After Calibration $\begin{pmatrix} Lu_L, Lu_R, \\ C_L, C_R \end{pmatrix}$	After Calibration (Lu_L)	After Calibration (Lu_R)	After Calibration (C_L)	After Calibration (C_R)
Feature ID				RMSE (m)				
Reflective Boards								
Board 0	24,659	0	0.186	0.018	0.019	0.018		
Board 1	131,216	0	0.051	0.016	0.018	0.015		
Board 2	16,768	0	0.189	0.018	0.017	0.018	NA	
Board 3	131,230	0	0.083	0.017	0.017	0.016		
Board 4	19,521	0	0.200	0.021	0.019	0.023		
Board 5	10,839	0	0.111	0.014	0.014	0.013		
Board 6	116,664	115	0.143	0.021	0.017	0.024		
Board 7	115,692	124	0.140	0.025	0.021	0.029	Avg. RMSE for point-based adjustment = 0.022	Avg. RMSE for point-based adjustment = 0.024
Board 8	111,134	118	0.137	0.025	0.021	0.029		
Board 9	106,437	119	0.140	0.024	0.019	0.029		
Board 10	107,613	116	0.137	0.027	0.023	0.032		
Board 11	109,326	116	0.139	0.025	0.020	0.029		
Ground/Wall Patches								
Ground 0	727,744	0	0.158	0.018	0.021	0.015		
Ground 1	782,376	0	0.146	0.022	0.024	0.020	NA	
Ground 2	887,971	0	0.336	0.022	0.020	0.023		
Wall 0	198,900	0	0.091	0.027	0.025	0.029		
Hut Ridges								
Ridge 0	20,810	121	0.262	0.019	0.019	0.017	0.025	0.023
Ridge 1	14,573	139	0.296	0.023	0.020	0.018	0.024	0.030
Light Poles								
Pole 0	214,102	0	0.079	0.021	0.022	0.023	NA	
Pole 1	159,808	0	0.077	0.022	0.022	0.022		

points in images belonging to different calibration primitives. An optimal representation and pairing scheme between imagery and LiDAR data were developed for points, linear features, and planar features by estimating the point definition redundancy that quantifies the contribution of a point pair toward system calibration. The proposed iterative calibration method is capable of deriving accurate estimates for the mounting parameters, even if the initial estimates for the scaling factors of image points or mounting parameters are considerably inaccurate. The proposed calibration strategy is observed to reach an accuracy that is better than the expected accuracy based on the accuracies of the hardware involved for each of the mobile mapping platforms. Moreover, the usage of linear and planar features for calibration makes the proposed strategy more practical as this allows for its implementation using various outdoor features, such as building facades, rooftops, building edges, ground patches, light poles, traffic signs, and so on. Future work will focus on developing an algorithm for automated identification and extraction of calibration primitives. Moreover, combining the mounting parameters (i.e., extrinsic parameters) and sensor parameters (i.e., intrinsic parameters) to obtain a comprehensive calibration leading to even more accurate point clouds. A thorough analysis needs to be conducted in order to derive an optimal/minimal configuration of tracks and target primitives in order to attain an accurate calibration of the intrinsic sensor parameters and extrinsic parameters simultaneously. Also, calibrated LiDAR and camera systems can be used to integrate the point clouds obtained from imagery and LiDAR data together in order to obtain colorized point clouds, which would facilitate a more accurate and reliable object or feature extraction techniques.

REFERENCES

[1] U. Weiss and P. Biber, "Plant detection and mapping for agricultural robots using a 3D LiDAR sensor," *Robot. Auton. Syst.*, vol. 59, no. 5, pp. 265–273, 2011.

[2] H. Lin *et al.*, "Semantic decomposition and reconstruction of residential scenes from LiDAR data," *ACM Trans. Graph.*, vol. 32, no. 4, 2013, Art. no. 66.

[3] K. Williams, M. J. Olsen, G. V. Roe, and C. Glennie, "Synthesis of transportation applications of mobile LiDAR," *Remote Sens.*, vol. 5, no. 9, pp. 4652–4692, 2013.

[4] I. Puente, H. González-Jorge, J. Martínez-Sánchez, and P. Arias, "Review of mobile mapping and surveying technologies," *Measurement*, vol. 46, no. 7, pp. 2127–2145, 2013.

[5] A. F. Habib, A. P. Kersting, A. Shaker, and W.-Y. Yan, "Geometric calibration and radiometric correction of LiDAR data and their impact on the quality of derived products," *Sensors*, vol. 11, no. 9, pp. 9069–9097, Sept. 2011.

[6] G. Atanacio-Jiménez *et al.*, "LIDAR velodyne HDL-64E calibration using pattern planes," *Int. J. Adv. Robot. Syst.*, vol. 8, no. 5, pp. 70–82, Nov. 2011.

[7] C. Glennie *et al.*, "Compact multipurpose mobile laser scanning system—Initial tests and results," *Remote Sens.*, vol. 5, no. 2, pp. 521–538, Jan. 2013.

[8] N. Muhammad and S. Lacroix, "Calibration of a rotating multi-beam LiDAR," in *Proc. 2010 IEEE/RSJ Int. Conf. Intell. Robots Syst.*, 2010, pp. 5648–5653.

[9] M. He, H. Zhao, F. Davoine, J. Cui, and H. Zha, "Pairwise LiDAR calibration using multi-type 3D geometric features in natural scene," in *Proc. 2013 IEEE/RSJ Int. Conf. Intell. Robots Syst.*, 2013, pp. 1828–1835.

[10] J. Weng, P. Cohen, and M. Herniou, "Camera calibration with distortion models and accuracy evaluation," *IEEE Trans. Pattern Anal. Mach. Intell.*, vol. 14, no. 10, pp. 965–980, Oct. 1992.

[11] Z. Zhang, "A flexible new technique for camera calibration," *IEEE Trans. Pattern Anal. Mach. Intell.*, vol. 22, no. 11, pp. 1330–1334, Nov. 2000.

[12] A. F. Habib, M. Morgan, and Y.-R. Lee, "Bundle adjustment with self–calibration using straight lines," *Photogramm. Rec.*, vol. 17, no. 100, pp. 635–650, 2002.

[13] Y. Furukawa and J. Ponce, "Accurate camera calibration from multi-view stereo and bundle adjustment," *Int. J. Comput. Vision*, vol. 84, no. 3, pp. 257–268, Sept. 2009.

[14] R. Delara, E. A. Mitishita, and A. Habib, "Bundle adjustment of images from non-metric CCD camera using LiDAR data as control points," in *Proc. Int. Arch. XXth ISPRS Congr.*, 2004, pp. 13–19.

[15] A. Habib, M. Ghanma, M. Morgan, and R. Al-Ruzouq, "Photogrammetric and LiDAR data registration using linear features," *Photogramm. Eng. Remote Sens.*, vol. 71, no. 6, pp. 699–707, Jun. 2005.

[16] Q. Zhang and R. Pless, "Extrinsic calibration of a camera and laser range finder (improves camera calibration)," in *Proc. 2004 IEEE/RSJ Int. Conf. Intell. Robots Syst.*, vol. 3, 2004, pp. 2301–2306.

[17] V. Fremont and P. Bonnifait, "Extrinsic calibration between a multi-layer LiDAR and a camera," in *Proc. 2008 IEEE Int. Conf. Multisens. Fusion Integr. Intell. Syst.*, 2008, pp. 214–219.

[18] J. Castorena, U. S. Kamilov, and P. T. Boufounos, "Autocalibration of LiDAR and optical cameras via edge alignment," in *Proc. 2016 IEEE Int. Conf. Acoust., Speech Signal Process.*, 2016, pp. 2862–2866.

[19] Q. V. Le and A. Y. Ng, "Joint calibration of multiple sensors," in *Proc. 2009 IEEE/RSJ Int. Conf. Intell. Robots Syst.*, 2009, pp. 3651–3658.

[20] J. Levinson and S. Thrun, "Automatic online calibration of cameras and lasers," *Robot. Sci. Syst.*, vol. 2, pp. 29–36, Jun. 2013.

[21] A. Dhall, K. Chelani, V. Radhakrishnan, and K. M. Krishna, "LiDAR-camera calibration using 3D-3D point correspondences," arXiv preprint arXiv:1705.09785, 2017.

[22] F. M. Mirzaei, D. G. Kottas, and S. I. Roumeliotis, "3D LiDAR–camera intrinsic and extrinsic calibration: Identifiability and analytical least-squares-based initialization," *Int. J. Robot. Res.*, vol. 31, no. 4, pp. 452–467, 2012.

[23] A.-I. García-Moreno, J.-J. Gonzalez-Barbosa, F.-J. Ornelas-Rodriguez, J. B. Hurtado-Ramos, and M.-N. Primo-Fuentes, "LIDAR and panoramic camera extrinsic calibration approach using a pattern plane," in *Proc. Mexican Conf. Pattern Recog.*, 2013, pp. 104–113.

[24] C. X. Guo and S. I. Roumeliotis, "An analytical least-squares solution to the line scan LiDAR-camera extrinsic calibration problem," in *Proc. 2013 IEEE Int. Conf. Robot. Autom.*, 2013, pp. 2943–2948.

[25] M. Vel'as, M. Španěl, Z. Materna, and A. Herout, "Calibration of RGB camera with Velodyne LiDAR," *J. WSCG*, vol. 2014, pp. 135–144, 2014.

[26] Z. Pusztai and L. Hajder, "Accurate calibration of LiDAR-camera systems using ordinary boxes," in *Proc. IEEE Conf. Comput. Vision Pattern Recog.*, 2017, pp. 394–402.

[27] V. Kubelka and T. Svoboda, "NIFTi LiDAR-camera calibration," *DR 22 Stereo- Omni-Directional Vision Hum.-Assist. Exploration*, 2011.

[28] Y. Park, S. Yun, C. S. Won, K. Cho, K. Um, and S. Sim, "Calibration between color camera and 3D LiDAR instruments with a polygonal planar board," *Sensors*, vol. 14, no. 3, pp. 5333–5353, 2014.

[29] A. R. Willis, M. J. Zapata, and J. M. Conrad, "A linear method for calibrating LiDAR-and-camera systems," in *Proc. 2009 IEEE Int. Symp. Model., Anal. Simul. Comput. Telecommun. Syst.*, 2009, pp. 1–3.

[30] L. Zhou and Z. Deng, "Extrinsic calibration of a camera and a LiDAR based on decoupling the rotation from the translation," in *Proc. 2012 IEEE Intell. Veh. Symp.*, 2012, pp. 642–648.

[31] G. Pandey, J. R. McBride, S. Savarese, and R. M. Eustice, "Automatic targetless extrinsic calibration of a 3D LiDAR and camera by maximizing mutual information," in *Proc. 26th AAAI Conf. Artif. Intell.*, 2012, pp. 2053–2059.

[32] S. Bileschi, "Fully automatic calibration of LiDAR and video streams from a vehicle," in *Proc. 2009 IEEE 12th Int. Conf. Comput. Vision Workshops*, 2009, pp. 1457–1464.

[33] X. Gong, Y. Lin, and J. Liu, "3D LiDAR-camera extrinsic calibration using an arbitrary trihedron," *Sensors*, vol. 13, no. 2, pp. 1902–1918, 2013.

[34] E. Renaudin, A. Habib, and A. P. Kersting, "Featured-based registration of terrestrial laser scans with minimum overlap using photogrammetric data," *ETRI J.*, vol. 33, no. 4, pp. 517–527, 2011.

[35] Applanix, "APX-15 UAV version 2, single board GNSS-inertial solution," 2016. [Online]. Available: https://www.applanix.com/downloads/products/specs/APX15_DS_NEW_0408_YW.pdf. Accessed on: Oct. 08, 2017.

[36] A. Habib, J. Lay, and C. Wong, "Specifications for the quality assurance and quality control of LiDAR systems," *Base Mapping Geomatics Serv. Brit. Columbia*, to be published, [Online]. Available: https://engineering.purdue.edu/CE/Academics/Groups/Geomatics/DPRG/files/LIDARErrorPropagation.zip. Accessed on: Dec. 20, 2017.

[37] M. Šenk and L. Cheze, "Rotation sequence as an important factor in shoulder kinematics," *Clin. Biomech.*, vol. 21, pp. S3–S8, 2006.

[38] A. Habib, K. I. Bang, A. P. Kersting, and J. Chow, "Alternative methodologies for LiDAR system calibration," *Remote Sens.*, vol. 2, no. 3, pp. 874–907, Mar. 2010.

[39] A. P. Kersting, A. Habib, and K. I. Bang, "Mounting parameters calibration of GPS/INS-assisted photogrammetric systems," in *Proc. 2011 Int. Workshop Multi-Platform/Multi-Sens. Remote Sens. Mapping*, 2011, pp. 1–6.

[40] Novatel, "Novatel SPAN-CPT user's manual," 2014. [Online]. Available: http://www.novatel.com/assets/Documents/Manuals/om-20000122.pdf. Accessed on: Feb. 20, 2017.

[41] Applanix, "POS LV 125 specifications," 2015. [Online]. Available: https://www.applanix.com/pdf/POS_LV_125_Data_Sheet.pdf. Accessed on: Oct. 08, 2017.

Radhika Ravi was born in India, in 1994. She received the B.Tech. degree in civil engineering and the B.Tech. degree in electrical engineering from the Indian Institute of Technology Kanpur, Kanpur, India, in 2016. She is currently working toward the M.S. degree in civil engineering (geomatics) at the Lyles School of Civil Engineering, Purdue University, West Lafayette, IN, USA.

Her research interests include 3-D point cloud reconstruction from LiDAR and photogrammetric data, intrinsic and extrinsic calibration of mobile LiDAR systems, and calibration of LiDAR systems integrated with several cameras.
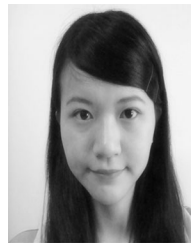
Yun-Jou Lin was born in Taiwan. She received the B.S. and M.S. degrees in civil engineering from the National Central University, Taoyuan, Taiwan, in 2011 and 2012, respectively. She is currently working toward the Ph.D. degree in geomatics at the Lyles School of Civil Engineering, Purdue University, West Lafayette, IN, USA.

Her current research interests include point clouds processing (i.e., segmentation, reconstruction, as well as feature extraction) from mobile mapping LiDAR system, terrestrial LiDAR systems, and image-based point cloud.

Magdy Elbahnasawy received the B.Sc. and M.Sc. degrees in electrical engineering from the Military Technical College, Cairo, Egypt, in 2004 and 2012, respectively. He is currently working toward the Ph.D. degree (interdisciplinary program "geo-electrical," which combines electrical and geomatics fields) at the Lyles School of Civil Engineering, Purdue University, West Lafayette, IN, USA.

His current research interests include multisensor integration for both terrestrial and aerial mapping systems, system calibration of LiDAR/imagery mapping systems, UAV-based 3-D mapping, as well as trajectory estimation in GNSS-denied areas using photogrammetric information.

Tamer Shamseldin received the B.S. and M.S. degrees in electrical engineering from the Military Technical College, Cairo, Egypt, in 2004 and 2012, respectively. He is currently working toward the Ph.D. degree in interdisciplinary program "geoelectrical" between geomatics at the Lyles School of Civil Engineering and Electrical and Computer Engineering, Purdue University, West Lafayette, IN, USA.

His current research interests include the development of system architecture for LiDAR-based UAV and terrestrial mapping systems, single and multi-LiDAR system calibration, and SLAM-assisted coverage path planning for indoor LiDAR mapping system.

Ayman Habib received the M.Sc. and Ph.D. degrees in photogrammetry from The Ohio State University, Columbus, OH, USA, in 1993 and 1994, respectively. He is currently a Professor in geomatics with the Lyles School of Civil Engineering, Purdue University, West Lafayette, IN, USA.

His research interests include the fields of terrestrial and aerial mobile mapping systems, modeling the perspective geometry of nontraditional imaging scanners, automatic matching and change detection, automatic calibration and stability analysis of low-cost digital cameras, utilizing low-cost imaging systems for infrastructure monitoring and biomedical applications, incorporating analytical and free-form linear features in various photogrammetric orientation procedures, object recognition in imagery, UAV-based 3-D mapping, as well as integrating photogrammetric data with other sensors/datasets (e.g., GPS/INS, GIS databases, multispectral sensors, and LiDAR).